UNIVERSIDAD CARLOS III DE MADRID

Experimental Analysis of Flapping Wings.

by

Ignacio Moreno Pubul

under supervision of

Stefano Discetti

Department of Bioengineering and Aerospace Engineering

September 2016

"Heisenberg was out for a Sunday drive on der landstrasse. He sees a police car with its lights on following him, so he pulls over. The policeman walks up, leans down to the window and asks, "Do you have any idea exactly how fast you were going?" Heisenberg responds, "No, but I do know exactly where I was!" The policeman says "You were doing 70 in a 50 km/h zone" "Well, thanks. Now I'm lost!""

-Unknown

UNIVERSIDAD CARLOS III DE MADRID

Abstract

Department of Bioengineering and Aerospace Engineering

Bachelor of Aerospace Engineering

by Ignacio Moreno Pubul
under supervision of Stefano Discetti

The development of this project is oriented towards the study of force coefficients and flow structures of a pitching and plunging airfoil at low Reynolds number. The experimental setup consisted of a NACA 0012 airfoil placed in a water channel. A motion system to control the airfoil allowed for a wide range of motion configurations. A waterproof Force/Torque sensor allowed capturing normal and axial forces, which were then be processed to obtain aerodynamic loads. The experiments were ran at a Reynolds number $Re = 3600$, Strouhal number $St = 0.2$, and reduced frequency $k = 0.1\pi$, with a fixed phase lag ϕ of 90° and plunging amplitude of $h_0/c = 1$ for all experiments. A total of six cases were performed, with varying pitching amplitude $\theta_0 = 0°$, 10° , 20°, and a mean pitch angle θ_m of 0° and 10° for each pitching amplitude. A PIV system was used to visualize and study the flow structures for two cases ($\theta_0 = 0°$, $\theta_m = 0°$; $\theta_0 = 20°$, $\theta_m = 10°$). Thrust production was only observed in cases with $\theta_m = 0°$, while an enhanced lift was noted in cases with $\theta_m = 10°$. Pitching amplitude seems to enhance lift and thrust production, specially the transition from $\theta_0 = 0°$ to $\theta_0 = 10°$. The analysis of PIV results rendered interesting results, namely the fundamental role of the leading edge vortex in lift production, and the effects of LEV and TEV shedding in drag evolution.

Acknowledgements

First and foremost, I would like to thank the faculty and staff of Universidad Carlos III de Madrid. Their work, day in and day out, makes it possible for all of us to expand the horizons of our minds and our dreams. All of us students thank you. A special mention in this aspect to Stefano Discetti, for his continuous support during the course of this thesis, and his help when help was due. I must also give credit to Marco Raiola, without his ingenuity, effort, patience and countless hours, despite the numerous attempts from Murphy to drag this project through time, this experiment would not have been possible. A mention also to Andrea Ianiro and Carlos Sanmiguel for their work in the hydrodynamic tunnel, and to the faculty of the Fluid Mechanics Laboratory, who kindly let us use their tunnel at the beginning stages of the experiments.

I could not go on without expressing my most sincere gratitude towards my friends and colleagues with whom I have shared the ups and downs of this adventure that we call University. The never ending projects, assignments and reports. Our football team, Olympique del Ion, with its victories and losses. The adrenaline filled examination weeks. Now we reach the conclusion to one of life's most interesting stages, so thank you for having been there.

Finally, I would like to thank the people who do not need to be thanked, because they know this is theirs as much as it is mine. My parents, for always pushing me to give all I have in every situation, and teaching me the values of life and love. To my brothers, Luis and Alvaro, and to my friends, they know who they are. To Myriam, for her unconditional support and friendship.

Contents

List of Figures

List of Tables

Abbreviations

Acronym	*Meaning*
2D	**T**wo **D**imensional
3D	**T**hree **D**imensional
NACA	**N**ational **A**dvisory **C**ommittee for **A**eronautics
MAV	**M**icro **A**ir **V**ehicle
UAV	**U**nmanned **A**erial **V**ehicle
LEV	**L**eading **E**dge **V**ortex
TEV	**T**railing **E**dge **V**ortex
TiV	**T**ip **V**ortex
PIV	**P**article **I**mage **V**elocimetry
CMOS	**C**omplementary **M**etal **O**xide **S**emiconductor

Symbols

k	reduced frequency	
St	Strouhal number	
Re	Reynolds number	
h	vertical position	m
h_0	Plunging amplitude	m
θ	pitch angle	$^\circ$, rad
θ_0	pitching amplitude	$^\circ$, rad
θ_m	mean pitch angle	$^\circ$, rad
f	flapping frequency	Hz
f_s	data sampling frequency	Hz
f_{cam}	camera capture frequency	Hz
ϕ	phase lag	$^\circ$, rad
T	period of oscillation	s
t	time	s
U_∞	free flow velocity	m/s
V	flow velocity	m/s
α_e	effective angle of attack	$^\circ$, rad
U_{ref}	reference velocity	m/s
L_{ref}	reference length	m
c	airfoil chord	m
b	wingspan	m
x_p	airfoil pivot point x-position	
S	airfoil surface area	m^2
ν	kinematic viscosity	m^2/s
ρ	fluid density	kg/m^3

L	lift	N
D	drag	N
C_L	lift coefficient	
C_D	drag coefficient	
C_T	thrust coefficient	
F_{aero}	aerodyamic forces	N
F_{mass}	mass forces	N
F_{buoy}	buoyancy forces	N
$F_{inertial}$	inertial forces	N
F_{X_B}	forces in body axes	N
N	normal force	N
A	axial force	N
n	number of cycles	
n_ϕ	number of phases per cycle	
n_{images}	number of images per phase point	
ϕ_{cycle}	phase within cycle	
X	horizontal position	m
Y	vertical position	m
U	horizontal velocity	m/s
X	vertical velocity	m/s
σ	standard deviation	

Chapter 1

Introduction

Many cultures, from the Mesopotamians to the Chinese dreamed of creating flying machines. Great minds such as Leonardo DaVinci tried to emulate the motion of birds wings in mechanical designs. However, it turns out the mechanics of the motion of natural flyers is extremely complex, and, even with today's technology, difficult to reproduce.

It was not until the 20th century that mankind finally achieved powered flight. However, the development of flying machines has focused on fixed or rotary wing devices, a lot more practical for heavy lifting, and a lot less complex than flapping wings. As humanity has learned to dominate human transportation through the air, new applications arise for the use of flying machines. Thus, as with many technologies before it, the aerospace industry is placing efforts on creating smaller, more efficient devices for day-to-day use.

Over the past few years, we have experienced the gradual introduction of flying machines as a relatively inexpensive, non-intrusive, common object. We are beginning to see drones and other unmanned aerial vehicles (UAVs) take to the skies for mapping and monitoring purposes. The agricultural industry is beginning to exploit the value of flying machines to yield more crops. Rescue and military services are using drones to monitor fires and find lost people. Even the entertainment industry is beginning to see a rise in commercial drones for media purposes.

Such a growth is accompanied by a new interest in the science community to improve the performance of these type of vehicles. And with it, flapping wing design may prove to be a new player in the industry, breaking the limitations of fixed and rotary wing aircraft. The performance of fixed wings deteriorates at low Re and such vehicles cannot sustain hover flight. Similarly, rotary wings do not work well at low scales, due to high profile and induced drag. Flapping wings present a superior solution in terms of efficiency and

lift generation, especially in hover. However, more work needs to be done to understand the effects that make them so effective.

Inspired by the 350 million year old technology developed by the best engineer on the planet, nature, micro air vehicles are being developed to out-do previous aircraft in terms of lift, thrust and control. We define micro air vehicles (MAVs) as aircraft whose weight is below 200 grams, and wingspan below 15cm. In the development of MAVs, fixed wing designs prove to be of little importance, as they need airflow over the surface of the wing to keep aloft. This diminishes the hovering capacities of the craft, and impedes proper control at low speeds. Rotary wings provide a better alternative. However, at low Reynolds number, characteristic of small aerial vehicles, where the flow field becomes more unsteady, rotor efficiency, especially during hover, is notably hindered.

In terms of efficiency and control, natural flyer performance, particularly insect flight, is beyond anything we have previously developed. Fruit flies for example are able to perform extremely precise banking and roll maneuvers, and make turns of close to 90° while undergoing accelerations of up to 9G. Even in terms of speed, even if it is just relative, some birds can greatly outperform even the most advanced fighter jets. The hummingbird, for example, can reach up to 383 body lengths. To put this into perspective, this would be like an F-22 flying at Mach 20 [6].

Naturally, insect wings are extremely complex, both in their motion and structural and elastic behavior. That is why in this experimental analysis, a simplified wing motion is utilized, consisting of an airfoil with variable pitch and plunge amplitude. The system is submerged in a hydrodynamic tunnel to study force generation in a pitching and plunging airfoil at a reasonable Reynolds number of 3600. By comparison, hawk moths, natural insect flyer widely studied for their size comparable to MAVs, display an Re in the range of 1150 to 5560 [7].

1.1 Document Structure

The document here presented is composed of 9 chapters. The goal of the structure is to walk the reader through the experimental process, from an introduction to the topic at hand to the results and their analysis. The chapters are defined as follows:

i. Chapter 1 serves as a general introduction to the project. History, background and state of the art, including a review of the most relevant literature and the current socioeconomic and legal frame. It also outlines the objectives of the project.

ii. Chapter 2 defines the problem in more depth. It establishes the kinematics of the experiment, the governing parameters and flow structures, as well as the forces at play. It is a theoretical introduction to the topic.

iii. Chapter 3 describes the experimental setup. It serves as an introduction to the wing motion system designed by Pablo Moral Maroto [8], the hydrodynamic channel at Universidad Carlos III de Madrid, and the force measuring setup and procedure. It also serves as an introduction to Particle Image Velocimetry equipment and setup.

iv. Chapter 4 explains the process that was followed in order to obtain raw forces, and the processing of this raw data into force coefficients necessary for proper analysis.

v. Chapter 5 goes into an in-depth review of the PIV image acquisition and processing procedure carried out to obtain a visualization of the flow.

vi. Chapter 6 serves as a compilation of the aerodynamic force results for each of the 6 experiments that were performed. The results are carefully analyzed and explained in this section.

vii. Chapter 7 describes the PIV experiments carried out for this project. It displays the results and explains the phenomenon in comparison with the theory described in previous chapters. It also contains a section dedicated to the correlation of PIV flow structures with the force results seen in Chapter 6.

viii. Chapter 8 serves as a closing statement, a conclusion of sorts for the information gathered through the development of the thesis.

ix. Chapter 7 describes the project planning and budget estimated for the development of the project.

The report is completed with an appendix, with results whose analysis do not necessarily add value, but that may result interesting nonetheless for the reader. The last pages contain the bibliography with complete sources.

1.2 Goals and Objectives

The overall goal of this project is to add value in the understanding of flow structures and their relationship with force generation in flapping wings. Within this framework, the following objectives have been defined:

i. Successfully setup the motion system, force measuring system, and PIV system in the new water channel at the Aerospacee Engineering Laboratory at Universidad Carlos III de Madrid. This includes calibration of the systems as well as identifying -and attenuating- sources of noise.

ii. Run six experimental cases, with varying pitching amplitude and mean pitch angle parameters, and capture, process and interpret the resulting aerodynamic loading evolution.

iii. Perform two PIV experiments and process the results to visualize and study the flow structures that appear in the pitching and plunging airfoil problem. These results can then be contrasted with the force coefficient evolution to correlate flow structures with force generation.

1.3 State of the Art

Before entering a deeper analysis of the work that was performed for this project, it is important to establish the framework in which it was developed. Previous important advancements in the field, as well as a socioeconomic summary of the topic can be found in the next few pages.

1.3.1 Literature Review

Understanding the underlying mechanics of natural flyers has been a topic of fundamental interest for the scientific community. Going as far back as the XV^{th}, with the famous designs of human powered flying machines by Leonardo DaVinci, there have been demonstrations of the appeal of this field. However, as powered flight took its first steps, the complexity of oscillating wing dynamics relegated mechanical flapping wing design to a secondary plane, and research was reduced to experimental activity and small-scale studies performed by some ornithopter inventors. Nonetheless, in the beginning of the 20^{th} century there were certainly some advancements.

To see the first studies on oscillatory wing motion, it is necessary to go back to 1909. Knoller [9] and Betz [10] were the first to propose that the motion of a flapping wing is characterized by an effective angle of attack. They noted that indeed an aerodynamic force was generated, and that this force, when decomposed into vertical and horizontal axes, yielded both a vertical lift, and a positive horizontal thrust, time-averaged from the upstroke and the downstroke. It was not until 1922 that Katzmayr [11] confirmed these results experimentally.

The following year, Birnbaum [12] published his findings on which he developed the first analysis of incompressible flow around oscillating airfoils utilizing linearized potential flow theory. This analysis was based on small disturbance theory, and thereby limited to small amplitude oscillations and planar wake. He also identified the importance of starting vortices at the trailing edge of the airfoil, a fact that was previously ignored by Knoller-Betz. In addition, he introduced the reduced frequency parameter, k, which compares the spatial wavelength of the flow disturbance with the chord length. It is one of the parameters that governs the oscillating airfoil problem.

$$k = \frac{\pi f c}{U_\infty} \tag{1.1}$$

where f is the frequency of oscillation, c is the chord length, and U_∞ is the free stream velocity.

Over the next decade, von Karman and Burger [13] published the first theories on thrust and drag generation of flapping wings. These theories were based on the position and orientation of vortices around the wake. In parallel, Theodorsen produced a result for incompressible potential flow in oscillating airfoils valid for the entire range of reduced frequency [14]. Applying the advancements pushed forward by von Karman, Burgers and Theodorsen, Garrick [15] predicted the thrust and propulsive efficiency of harmonically plunging or pitching airfoils. He recognized that pure pitching motions are only accompanied by thrust when a high value of frequency is reached.

In the 60's, Polhamus [16] described the effects of one of the most important flow structures in the oscillatory airfoil problem. In his work, he suggested that the Leading Edge Vortex (LEV) that forms over sharp-edge wings affects lift generation.

More recently, with the advent of computer simulations and more advanced imagery and equipment, coupled with the added interest for this type of flight, more progress has been made in the field. Many studies have been focused on the formation of vortex structures around the airfoil. The clear correlation between vortical structures and aerodynamic force generation has been a topic of discussion for quite some time.

Anderson et al. [17] placed harmonically oscillating NACA 0012 airfoils in a water tunnel at low Reynolds number to measure the thrust. They performed a study to find the best conditions for thrust production, and noted the formation of a reverse von Karman vortex street. This vortex street was formed by LEVs and Trailing Edge Vortices, TEVs, shedding from the trailing edge of the airfoil.

Similarly, Ellington et al. [18] performed research utilizing a robotic moth wing and smoke flow visualization. They developed a theory for the increased lift effect of Leading

Edge Vortices during the downstroke, determining a delayed stall effect as a probable cause of the increased lift [19]. Dickinson et al. [20] also performed similar experiments to find a relationship between aerodynamic forces and the kinematics of the flapping wing. They categorized the loading in three parts: delayed stall effect, rotation, and wake capture (interaction with the wake).

In 1993, Dickinson and Goetz [1] published experimental results for a pure plunge oscillation simulating hovering flight. The results shed some light on the critical function of LEVs to achieve high lift necessary for hovering flight. Zbikowsi [2] and Ansari et al. [3] used potential flow modeling to study the same problem, rendering very similar leading and trailing edge vortical structures, as seen on figure 1.1.

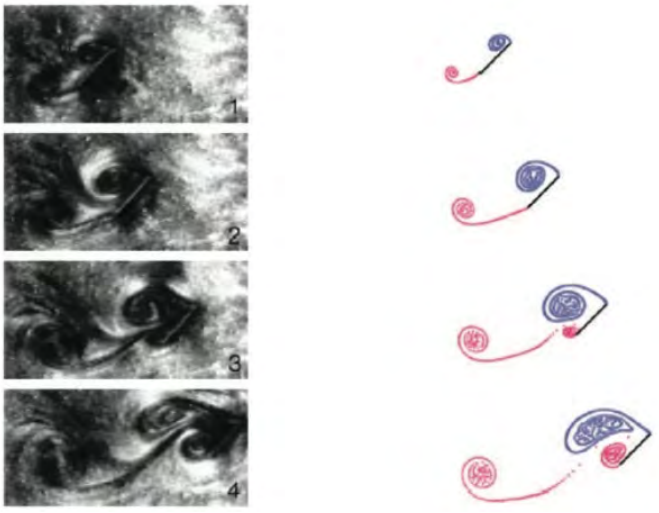

FIGURE 1.1: A comparison between experimental [1] and potential flow modeling [2] [3] results.

In the 2010's, Shyy et al. [21] reviewed the most recent advancements in flapping wing aerodynamics. He described findings in the formation of LEVs, their interaction with Trailing Edge Vortices (TEV), and Tip Vortices (TiV). He recognized the stability of the LEV as a critical parameter for lift contribution. In his 2013 book [22], he presents a thorough summary of the current theories, experimental results, and conclusions on the unsteady aerodynamics of flapping wings.

Sik Baik et al. [23], investigated the effect of non-dimensional parameters that dominate pitching and plunging airfoils, namely Strouhal number (St), and reduced frequency (k), for equal angle of attack kinematics. An experimental study of a pitching and plunging flat plate at low Reynolds number, with sinusoidal effective angle of attack motion was conducted. It was concluded that the formation of the LEV is strongly related to k, with delayed formation for increasing k. Instances with the same k showed that velocity profiles normal to the airfoil surface are quite similar in all cases regardless of pitch rate. In 2012 experiments [4], they reported the unsteady flow development, LEV vortex

dynamics and force generation in pitching and plunging flat-plates. It was confirmed that k plays a major role in LEV flow evolution, while St has a larger impact in force coefficient histories.

Pitt Ford and Babinski [24] carried out an experiment to determine the influence of LEV on lift generation. In their 2012 paper, they try to determine what proportion of the lift force is due to LEV effects. They concluded that lift is caused by external vortices and non-circulatory effects rather than the bound circulation of the wing, and that the slow build up of circulation contained in the LEVs contribute to lift generation.

1.3.2 Socioeconomic & Legal Frame

Scientific research and public interest on scientific topics is often powered by commercial success of certain technologies. When products or technological services become mainstream in the public eye, research on such advancements becomes well-funded, and the possibility to expand the horizons of said field is greatly expanded. This is the current case in the field of drones and other small aerial vehicles. In 2013, the global market for these type of devices did not even reach $50 million. Today, in 2016, the market reaches $552 million, and is expected to steadily grow at a 16% rate through 2022 [25].

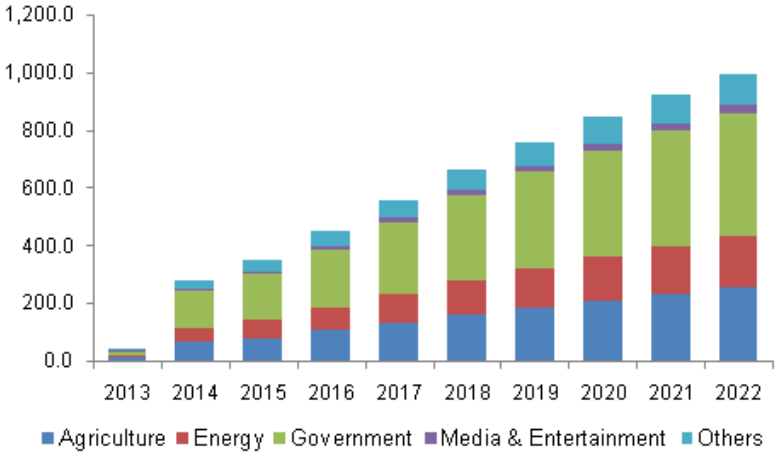

FIGURE 1.2: A look at the projected growth of the drone market until 2022.

The applications of these vehicles are wide. They are currently used in agriculture, government and military roles, energy, and of course mainstream commercial entertainment purposes. Crop monitoring is expected to become one of the main applications of drones, helping increase the agricultural yields over the next few years. However environmental monitoring, fire control and protection, rescue services are also growing. Even technological giants such as Google or Amazon are studying the use of drones for e-commerce applications [26].

There are also several types of unmanned aerial vehicles, each with their different applications. The most popular variations include fixed wing drones, rotary wing drones, micro air vehicles (MAVs) and hybrid drones. Work in flapping wings focuses more in the development of MAVs.

One of the more worrying parameters in current UAV technology is endurance, the time the vehicle can stay in the air. For the electric variants, battery life is one of the performance indicators that must improve for the success of drones to continue to grow. As the size of drones gets smaller and smaller, rotary wings lose efficiency, and thus perform poorly in terms of endurance. This is a problem when it comes to closed-space operations, where MAVs are the best choice of device, for example in urban rescue operations. Flapping wings, such as the ones seen in natural flyers (birds and insects) present themselves as a potential substitute for rotary wings, as they seem to offer greater efficiency, which translates to longer flight times. However, flapping wing dynamics are not yet fully understood. There is an opportunity in the field of aerodynamics to further investigate in this topic.

The potential socioeconomic reward is great. The drone industry could see huge growth, similar to the one observed in rotary wing drones, as MAVs applications increase with their increased efficiency. It is an opportunity for the aerospace industry to develop new tools to improve rescue, surveillance and monitoring operations, participating in the improvement of safety and rescue missions all over the world.

The current regulatory framework focuses mostly on drones and other aerial vehicles heavier than 0.5 pounds. The Federal Aviation Authority (FAA) and European Aviation Safety Agency (EASA) currently ban the use of UAVs for non-commercial purposes, and even limit the use of small rotary wing aircraft for entertainment purposes. However, MAVs, due to their light weight, are exempt from regulation, which means there is unrestricted development in this field. As of today, regulation should not affect research on flapping wing aerodynamics. However, as consumer drones reach the masses, regulation concerning MAVs and other small flying devices could become the norm.

Chapter 2

Problem Definition

This chapter is dedicated to a thorough introduction to the topic, complete with problem definition and basic concepts, defined over four sections. In the first section, the parameters of the flapping motion are defined and specified for this particular experiment. In the second, the governing parameters that affect the flow field and aerodynamic forces are also established. Along these lines, this chapter also serves as an introduction to the main vortical structures that affect the force coefficients (third section), as well as to the forces of interest in this project (fourth section).

2.1 Flapping Wing Kinematics

The kinematics of flapping wings in natural flyers is a rather complex motion, combining wing rotation, wing plunging and elasticity to generate the necessary aerodynamic effects that characterize their complex flight patterns. However, to understand the underlying unsteady aerodynamics, and study the basic flow structures, a much simpler motion is sufficient. The experiment is therefore based on a simpler flapping wing, a combination of pitching, or rotation, and plunging, vertical motion, as seen on figure 2.1.

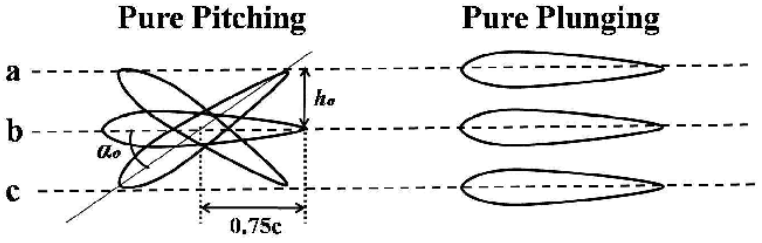

FIGURE 2.1: A combination of pitching and plunging motion; a flapping airfoil.

The kinematics of the flapping wing are defined by the parameters summarized in figure 2.2.

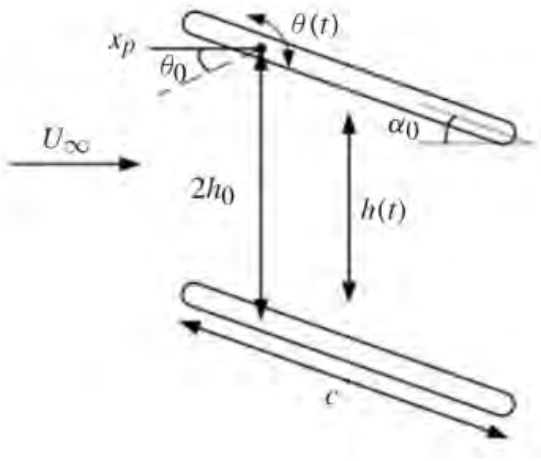

FIGURE 2.2: The kinematics of the flapping wing, or pitching-plunging aifoil. Image from [4].

The motion of the wing is characterized by a vertical plunging parameter, $h(t)$, and a pitching parameter $\theta(t)$, which is essentially the geometric angle of attack. The pitching rotation occurs about point x_p, which gives the distance of the pivot point from the leading edge.

The vertical motion depends only on h_0, the plunging amplitude (maximum vertical displacement above and below the rest position):

$$h(t) = h_0 sin(2\pi f t) \tag{2.1}$$

The pitching parameter depends on θ_0, the oscillation amplitude and θ_m, the mean pitch angle:

$$\theta(t) = \theta_m + \theta_0 sin(2\pi f t + \phi) \tag{2.2}$$

where f is the frequency of oscillation, t is time, and ϕ is phase lag between pitching and plunging motion. The cycle is thus divided in an upstroke and a downstroke of equal duration. The duration of the cycle is given by its period, T, which is defined as:

$$T = \frac{1}{f} \tag{2.3}$$

The following figure (2.3) shows one cycle of oscillation, where the sine wave is clearly visible:

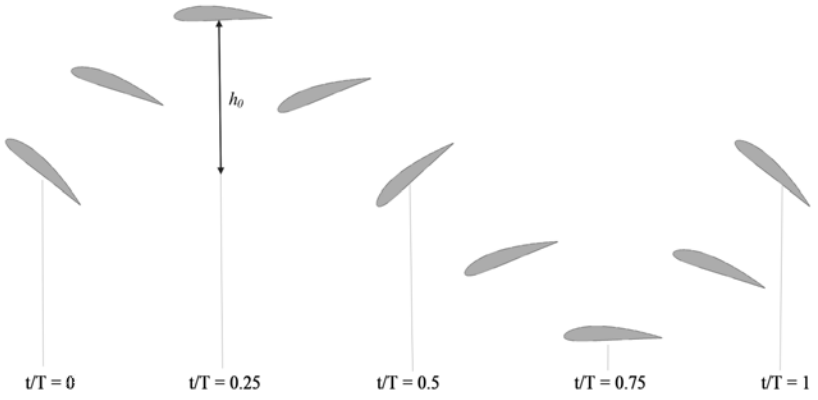

FIGURE 2.3: A diagram with the complete cycle of the oscillating airfoil using the previously defined kinematics. $\theta_0 = 40°$, $\theta_m = 0°$, $\phi = 90°$.

In unsteady flows such as this one, the angle with which the flow incises on the airfoil is not equal to the geometric angle of attack, and it varies due to the velocity of the airfoil through the fluid. Therefore, a useful parameter known as the effective angle of attack, α_e is defined:

$$\alpha_e = \theta(t) + atan(\frac{-\dot{h}(t)}{U_\infty}) \tag{2.4}$$

where $\theta(t)$ is the geometric angle of attack, and $\dot{h}(t)$ is the plunge velocity. In essence, α_e is the angle formed by the airfoil and the incoming stream for an observer moving with the pivot point.

2.2 Governing Parameters

Scaling laws help reduce the number of parameters, and determine the ones that stand out in a given condition. This can help set model standards for studying the aerodynamics of oscillating airfoils.

The main dimensionless parameters that govern the experiment are the Reynolds number, Re, Strouhal number, St, and reduced frequency, k. Each one of these parameters affects the flow structures or aerodynamic forces in a different manner:

i. **Reynolds number** is the ratio between inertial forces and viscous forces. Given a reference length, L_{ref}, and a reference velocity, U_{ref}, Re is expressed as:

$$Re = \frac{U_{ref} \cdot L_{ref}}{\nu} = \frac{U_\infty \cdot c}{\nu} \tag{2.5}$$

For the flapping wing problem, it is common to take the chord c of the wing as L_{ref}, because the flapping wing generates the lift and thrust. In the forward flight case, the free stream velocity U_∞ is taken as U_{ref}.

ii. **Strouhal number** compares the relative importance of free stream velocity U_∞ with the flapping speeds. It characterizes the shedding of vortices, as well as the dynamics of the vortical structures in the wake. In oscillating airfoils, it is expressed as:

$$St = \frac{fL_{ref}}{U_{ref}} = \frac{2fh_0}{U_\infty} \tag{2.6}$$

where f is the oscillation frequency of the wing and h_0 the oscillation amplitude.

Natural flyers in forward flight tend to display St in the range of $0.2 < St < 0.4$. Strouhal number seems to be an interesting parameter in force generation. Therefore, isolating St can be useful to study how it affects aerodynamic loading. However, changing St modifies α_e, so to isolate its effect, it is necessary to preserve effective angle of attack history for all St [23].

iii. **Reduced frequency**, k, offers a manner of defining the degree of unsteadiness of the problem. In forward flight, it is defined as:

$$k = \frac{\pi f c}{U_\infty} \tag{2.7}$$

It presents a better representation of the unsteadiness of the flow than St.

Table 2.1 serves as a reference to the dependency of these fundamental parameters to scaling parameters:

Dimensionless Parameters	*Length*	*Velocity*	*Frequency*
Reynolds Number, Re	c	U_∞	Independent
Strouhal Number, St	c	U_∞^{-1}	f
Reduced Frequency, k	c	U_∞^{-1}	f

TABLE 2.1: Scaling: dimensionless parameters and their dependency to experimental variables.

2.3 Flow Structures

The flapping wing problem is largely determined by the unsteady aerodynamic mechanisms that govern the flow. The study of these mechanisms is crucial to understand the structures that maximize lift and thrust. The main structures that govern the flow are leading edge vortices (LEVs), trailing edge vortices (TEVs), and tip vortices (TiVs), although these last structures are 3D effects and therefore outside the scope of this project.

To visualize these structures, Particle Image Velocimetry experiments will be performed for two different cases.

2.3.1 Leading Edge Vortices

LEVs are the most important structures in terms of lift enhancement in flapping wings.

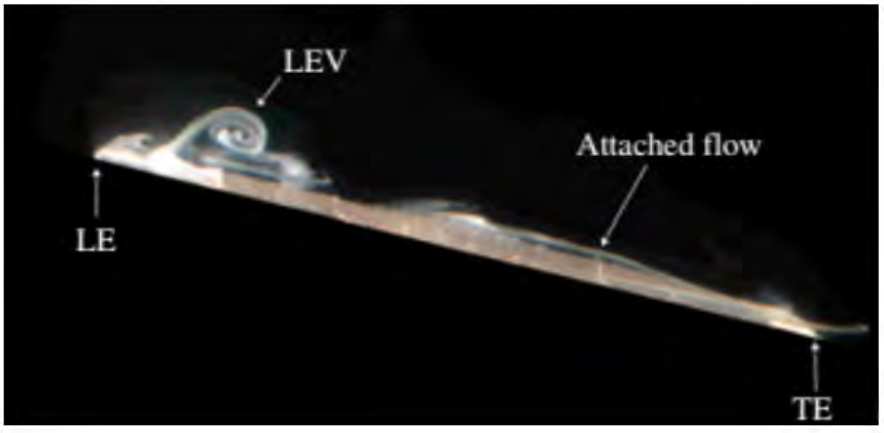

FIGURE 2.4: An image showing a smoke visualization of the LEV clearly forming over the leading edge of the wing.

The formation of the LEV is observed during the downstroke motion of the wing, as the flow detaches when the wing travels several chord lengths. It is characterized by a region of strong vorticity delimited by a streamline that ends on the surface of the airfoil.

The slow build up of circulation contained in the LEVs contributes to lift generation. The LEV produces low-pressure zone on the upper region of the wing, increasing lift. The stability of this vortex is essential to delay stall and increase lift. This "Delayed Stall Effect" has been thoroughly observed in literature, rendering approximately 3 times higher lift during downstroke than upstroke [21]. Figure 2.6 shows the mechanics of LEV force generation.

With appropriate adjustment of the airfoil motion, it should be possible to gradually feed the leading edge vortex, making it more stable. Part of the objective of this project

is to test several cases with different kinematic parameters, such as pitching amplitude and mean pitch angle, to determine the best configuration for lift and thrust.

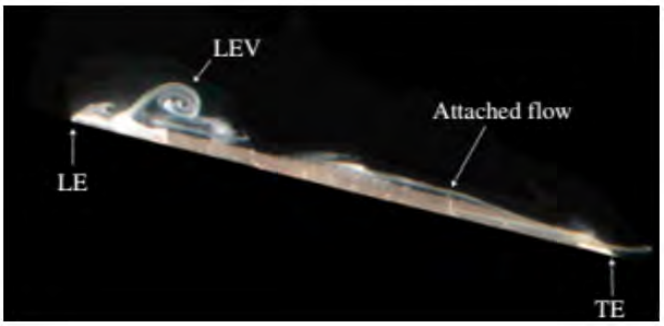

FIGURE 2.5: An image showing a smoke visualization of the LEV clearly forming over the leading edge of the wing.

The LEV is dependent not only on the kinematic parameters of the motion, but also on the governing parameters of the flow discussed in 2.2.

Reduced frequency, k, appears to be the governing parameter in LEV formation. Higher k induces a delay in the formation of the LEV. As k increases, growth rate decreases. It also affects LEV area: higher k decreases area [4].

Strouhal number, St, also has influence on the flow structure. Higher St generates a higher circulation. However, its effect is less relevant than that of k. Also, it appears not to affect LEV area.[4]

Reynolds number plays a role as well. In low Reynolds number regime, viscosity quickly dissipates the structures.

2.3.2 Trailing Edge Vortices

To compensate the growing circulation in the leading edge vortex, vorticity is produced at the trailing edge. As the flow develops, the LEV convects downstream . When the flow reattachment point reaches the trailing edge of the airfoil, and the LEV begins to separate, the built up vorticity is shed producing a trailing edge vortex.

In general, TEVs are seen as detrimental to lift production, although in hovering flight it is possible that they help keep the LEV attached.

In order to reduce the negative effects of the TEV, it is possible to perform a quick pitch motion in the transition from upstroke to downstroke, reducing the development of the trailing edge vortex.

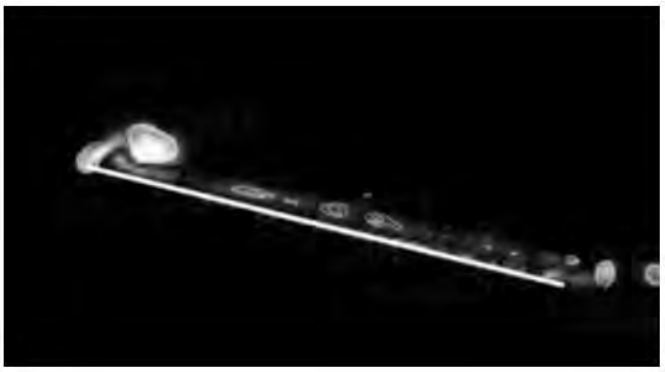

FIGURE 2.6: An image showing a smoke visualization of an airfoil displaying an LEV and TEVs.

2.3.3 Tip Vortices

Like LEVs and TEVs, Tip Vortices are also formed during the movement of the wing through the fluid. They are a strictly 3D effect, associated with finite wings. They must be mentioned because although the experiment is analyzed as a 2D experiment, it is a finite wing inside a hydrodynamic tunnel, and so 3D effects are expected. They are small in comparison to the standard aerodynamic forces, so they are not accounted for.

TiVs impact forces by generating a low pressure zone, interacting with LEV s or affecting the wake structure. In flapping motion in hover, they can either promote or have little effect on aerodynamic forces [21].

2.4 Forces

The other important aspect within the scope of this project is analyzing the aerodynamic force coefficients for cases with different kinematic parameters.

Naturally, lift, drag and thrust are the interesting coefficients for this analysis. The measurements however render axial (chordwise) and normal force on the plate. As will be explained later, a transformation from body axis to a reference frame aligned with the tunnel is necessary to attain lift and drag.

Normal forces are an order of magnitude stronger than axial forces, which suggests friction and LE suction effects are small compared to normal pressure force [4].

2.4.1 Lift

Since geometric angle of attack is relatively small throughout the experiment, lift is dominated by normal force on the airfoil. St is the largest contributor to normal force change. Normal force increases with St. Hence, lift is also governed by Strouhal number. Reduced frequency also plays a role in lift evolution, delaying the increase in lift coefficient for higher k values. Effect of the Reynolds number is small.

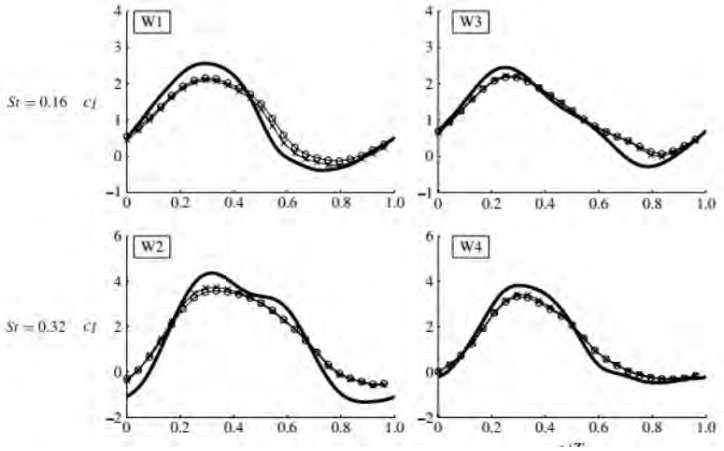

FIGURE 2.7: C_L results as a function of t/T, for different St values. From [4].

Larger lift values are associated with the downstroke motion of the wing as St is increased. C_L may reach values notably higher that the $2\pi\alpha_e$ expected in steady theory. The peaks in lift are located at the middle of the downstroke motion, where effective angle of attack is maximum.

2.4.2 Thrust and Drag

Another objective of this project is to study configurations which may produce thrust, rather than drag that would be expected from static airfoils.

At certain Strouhal numbers, the pitching and plunging airfoils produce forward thrust. This occurs when the vortices in the wake display a flow structure similar to the von Karman vortex street, but with reversed direction of vorticity. These vortex structures are called reverse von Karman vortices. The transition from standard to reverse von Karman street is illustrated in figure 2.8.

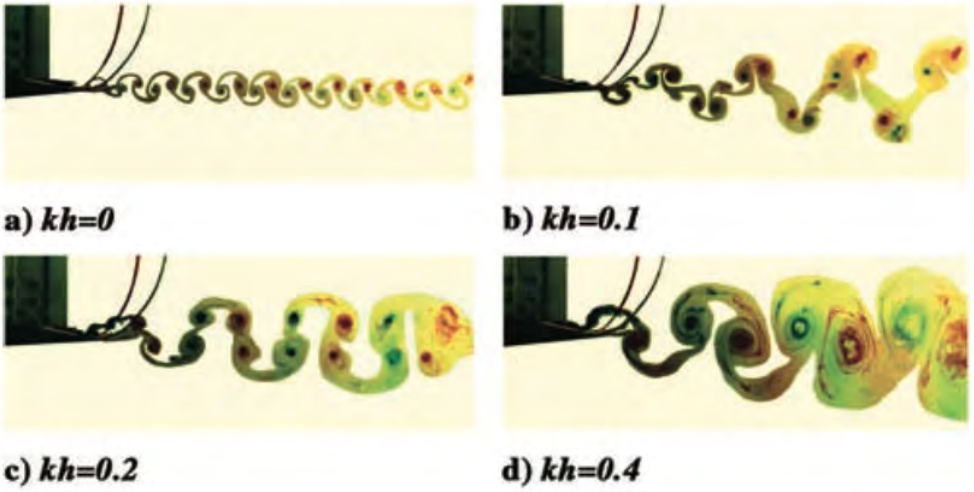

FIGURE 2.8: Transition from von Karman to reverse von Karman wake structure. From [5].

The figure shows vortex shedding from a pure-plunging airfoil. The upper row in the reverse Karman vortex street (i.e. bottom-right image) shows counterclockwise rotating vortices, while the lower row has clockwise vortices. Thus, the flow is is pushed between the rows, such that its velocity distribution is that of a jet. The oscillation therefore creates, as a reaction, a thrust on the airfoil.

Chapter 3

Experimental Setup

This chapter serves as a review of the experimental setup of the flapping wing . It is comprised of four sections. In the first one, the wing motion system and its components are described. The second section briefly describes the force measuring equipment. The third one is a brief introduction to the hydrodynamic tunnel. The fourth and final section explains the PIV setup.

3.1 Wing Motion System

The wing motion system designed by Pablo Moral Maroto [8] was utilized for this experiment. The system is composed of two moving rods, each coupled with a linear actuator and an AC motor. The function of the rod system is to convert the linear motion of the actuators to the pitching and plunging motion needed for the flapping wing.

The wing-end of the rod system has a three-joint system, on which the F/T force and torque measuring sensor is attached. The wing is then attached to the sensor with three screws. It is placed centered with respect to the water tunnel's vertical axis, to minimize wall effects, and with a 5 mm clearance between the walls and the tips of the wing.

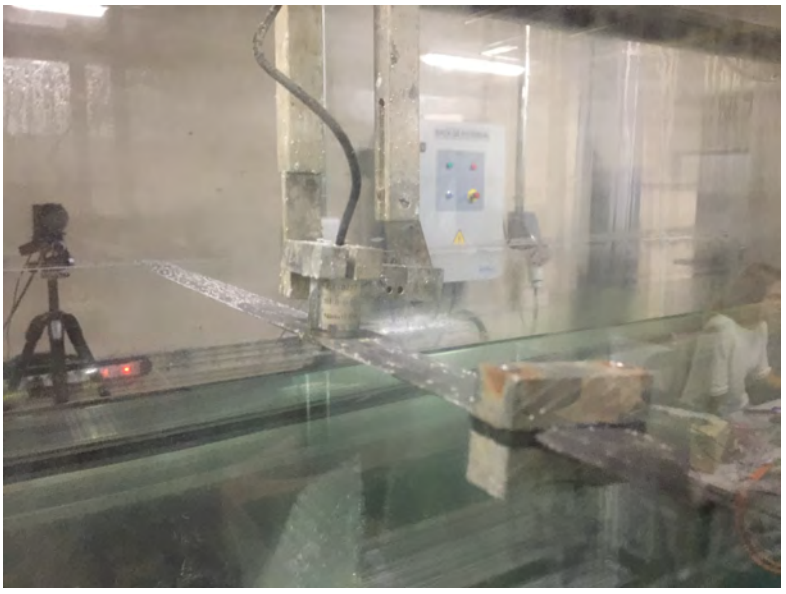

FIGURE 3.1: Wing assembly in the water channel experimental chamber.

Each of the motors is controlled by Festo CMMP-AS-C2-3A-M0 controllers, which also serve as power supply units for the synchronous Festo EMME-AS-40-M-LV-ASB motors.

The controllers are interfaced with the user through an Analog Discovery I/O device manufactured by Digilent. This is the device that is actually in communication with the computer, which is running a Python script with the kinematics of the rod system, which allows to set a specific motion to run the experiments. This I/O device can also be used to synchronize the high speed camera for PIV experiments.

The motion system was originally mounted on the water channel at the Fluid Dynamics Laboratory. It had to be disassembled, transported to the new water channel at the Aerospace Department Laboratory and reassembled over the new tunnel. The larger tunnel offers a wider separation from top and bottom wall, dissipating wall effects, and allows a wider wingspan, so the problem is closer to 2D. An aluminium mounting rod structure was built around the channel with a double objective: first, to mount the motion system over the top tunnel opening. This process required several modifications and adjustments with neoprene tape, as well as careful laser alignment in all three axis' to ensure the airfoil was as best aligned as possible. Second, to mount the high-power laser and the light sheet optics below the tunnel, to illuminate the experiment for PIV.

FIGURE 3.2: Motors and actuators for the wing motion system. Plexiglas lid with opening for rods.

In addition, some modifications had to be performed on the Plexiglas closing lid to ensure sufficient sealing to pressurize the system. The modifications included a 45° edge cut to facilitate the opening and closing of the system, for better access to the wing assembly, and an opening for the rods of the motion system.

FIGURE 3.3: Aluminum frame supporting the laser and laser optics.

3.2 Force Measuring Equipment

Force and torque data are captured by an ATI Industrial Automations Nano-17 IP68 waterproof 6-axis sensor. The sensor is placed on the motion system horizontal rod, with the airfoil attached directly to it with three screws.

Worth noting is that a counterweight had to be placed a one end of the wing to avoid torque saturation. This can be seen, along with the sensor itself with the assembled wing, in figure 3.1.

The force measuring system is completed with an interface and power supply box, and National Instruments Data Acquisition hardware. The F/T sensor is connected to the interface and power supply box, which is in turn connected to the data acquisition device. This device is finally connected to the computer, running a custom LabView program that controls measuring parameters, such as sampling frequency.

To synchronize data capture with the motion system, the data acquisition hardware has a trigger, in sync with the clock of the motion system.

3.3 Hydrodynamic Tunnel

The hydrodynamic tunnel at the Aerospace Engineering laboratory at UC3M is a state of the art water tunnel and channel designed and built by VTI S.L. an engineering firm based in Leganes, Madrid. The total dimensions of the tunnel are 10x3.8x2.5 (length, width, height, in meters), with an empty weight of 2200 kg. It holds approximately 10.000 litres of water.

The testing chamber where experiments are carried out is 2.5 meters long, by 0.5 meters wide and 0.5 meters tall. It can reach flow velocities of up to 1 m/s, with a turbulence intensity of less than 1.5%.

FIGURE 3.4: Experiment chamber of the hydrodynamic tunnel, with the aluminium frame for PIV and motion system..

The testing section also has sufficient space and structural integrity to hold the necessary instrumentation for different experiments, in this case for the wing motion system.

The channel can be controlled with a PC installed in the laboratory, connected to the control cabinet.

3.4 Particle Image Velocimetry

During the development of the experiment, Particle Image Velocimetry (PIV) was used for two main purposes. First, to determine the velocity of the free flow stream, and second, to study the velocity fields and flow structures around the flapping wing.

The working principle behind PIV is the slight change in the position of suspended particles in a known timeframe. This system allows for the computation of velocity vectors and to obtain the velocity field of large areas.

In its essence, the PIV system is relatively simple. The fundamental PIV system, the basic planar system utilized in this experiment, takes images from a single 2-D plane. By using optics, a laser is used to illuminate the particles in a plane, which must be carefully focused with the camera system. The result is the 2-D velocity field of the illuminated section.

The great advantage of this system is it allows to obtain both qualitative and quantitative data without interfering with the flow itself. Because it is an optical system, the flow is

not interrupted by measuring tools such as pitot tubes. The effect of the particles can be neglected due to the negligible concentration. The qualitative side of the experiment is related to flow visualization. Using PIV, the user is able to obtain a freeze-frame of the flow at any given time. Flow structures, such as von Karman vortices, TEVs and LEVs can be observed using the system. Current technology also enables obtaining quantized information, such as velocity fields, and vorticity contours of whole field areas, not just a single point.

The PIV system has several components that need to be setup to perform the experiment.

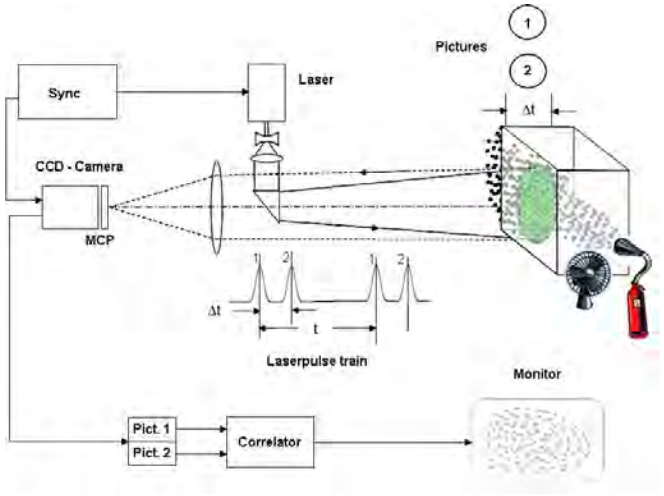

FIGURE 3.5: Typical experimental setup for particle image velocimetry.

3.4.1 Double Pulsed Laser

As shown in the introduction to the tunnel, section 3.3, the aluminium frame built around the hydrodynamic tunnel included a module to mount the high powered laser.

Only laser light can be focused with the necessary thickness to be considered a plane, necessary condition for PIV procedures. In addition, laser light has the sufficient energy for the illumination of the particles to be enough to form visible images. This energy can range from 5 to 500 mJ, depending of the scattering properties of the chosen particles.

PIV lasers usually contain a pair of lasers in a single housing, that enable the double pulse needed to capture the very quick sequence of image pairs necessary to build the velocity fields.

The laser utilized is a Quantel EverGreen, with an energy of $200mJ/\text{pulse}$, and a maximum frequency of 15 Hz.

There are some safety regulatory concerns when working with such high powered lasers. It is imperative to keep safety in mind. When the experiment is running, the hydrodynamic tunnel must isolated from the rest of the laboratory with an opaque sheet, pictured in figure 3.4, and safety goggles that filter out the laser frequencies are mandatory to avoid serious eye damage.

3.4.2 Seeding Particles

Naturally, the flow medium must be seeded with tracer particles. These particles can have different natures: droplets, bubbles or solid particles are common options. The role of the particles is to scatter the light coming from the laser, providing the camera system with something to trace.

The two main parameters associated with seeding particles are size and quantity. The size of the particles is crucial for the experiment. If the particles are too small they will not scatter enough light and the image quality will be low. If, in contrast, the particles are too large they may not properly follow the flow due to their higher momentum. Standard sizes range from 10 to 100 μm. Similarly, too few particles will render inaccurate data due to poor resolution, while too many will result in inaccurate results due to poor correlation during processing, as individual particles cannot be differentiated.

Material properties are also important. To counteract the influence of gravity with buoyancy forces, they should have a similar density to the fluid medium. In this experiment, poly-amide particles, with a diameter of 65 μm, are utilized.

3.4.3 Image Capturing Equipment

Image capturing is performed with scientific complementary metal-oxide-semiconductor (sCMOS) cameras. For 2-D flows, such is the case here, a single camera setup is sufficient. In older systems, cameras could not capture the two pulses of light in separate frames because they were not fast enough. Instead, they captured both pulses in a single frame. This led to inaccuracies, as it was difficult to tell which particle position belonged to the first pulse, and which to the second.

With this camera however, the two pulses can be captured in separate frames, one immediately after the other, removing this uncertainty and enabling cross-correlation signal processing.

The camera used for the experiment is an Andor Zyla 5.5 sCMOS scientific camera.

Laser pulses and image capturing must be carefully synchronized to obtain reliable results. The image capturing process occurs at an extremely fast rate: the time between frames is of only 4 ms. At these time scales, equipment must be very precise to avoid any errors in the measurements.

Choosing the time between laser pulses, and thus frame capture δt is one of the challenges of performing a PIV experiment. This parameter is usually chosen a function of the free stream velocity, particle size, and characteristics of the flow. If the δt is too short, the movement of the particles will be too small, and thus relative error large. On the other hand, if too much time passes between frames, the particles will have moved too much. This will generate errors on two fronts: firstly, because particles may not follow a linear path, and secondly, because even though the flow is mostly 2D, there may be some slight 3D effects which push particles in and out of plane. Leaving too much time between frames will maximize these errors.

The timing is usually chosen to correspond with one or two particle diameters.

Chapter 4

Force Acquisition and Processing

This chapter is dedicated to the acquisition and processing of the force data that will later be presented in the results. It defines the acquisition process of raw forces, as well as the different steps that must be followed to turn the raw data in usable information: aerodynamic force coefficients.

4.1 Raw Force Capture

The F/T sensor measures the forces and torques in a raw form, that is, the entirety of the forces that act on it, including mass, buoyancy, and inertial forces. Therefore, isolating the aerodynamic force is required.

The total force acting on the sensor can be written as:

$$\vec{F}_{tot} = \vec{F}_{aero} + \vec{F}_{buoy} + \vec{F}_{mass} + \vec{F}_{inertial} \tag{4.1}$$

where $\vec{F}_{aero}$ are the aerodynamic forces, $\vec{F}_{buoy}$ buoyancy forces, $\vec{F}_{mass}$ are the forces due to the mass of the wing, and $\vec{F}_{inertial}$ are the inertial forces.

Thus, to compute aerodynamic forces, simply:

$$\vec{F}_{aero} = \vec{F}_{tot} - \vec{F}_{buoy} - \vec{F}_{mass} - \vec{F}_{inertial} \tag{4.2}$$

In order to obtain these values, four different experiments need to be run:

i. To obtain $\vec{F}_{tot}$ a dynamic experiment (normal flapping frequency, f) with the full tunnel running at U_∞. In terms of the experiment, it is $\vec{F}_{U_\infty,f}$.

ii. To acquire $\vec{F}_{mass} + \vec{F}_{buoy}$, a static experiment (reduced f, or f_{static}) with the full tunnel at V = 0 m/s so as to not generate aerodynamic force. Because the sensor moves with the wing, these forces change with pitching angle. This static experiment thus takes the forces at all pitching angles, while the reduced flapping speed ensures no aerodynamic force is generated due to relative motion of the airfoil through the fluid. This experiment generates $\vec{F}_{V_0,f_{static}}$. In addition, the sensor is affected by the depth, which changes throughout the experiment; running the static experiment also removes this error.

iii. Inertial forces are forces generated due to the acceleration of the wing during the flapping motion. To compute $\vec{F}_{inertial}$, two more experiments are required. They are identical to the previously described experiments, a dynamic case (with f), and a static case (with f_{static}), but with an empty tunnel. Each experiment will eliminate the inertial forces of its full tunnel analogous. The purpose of the empty tunnel is to generate negligible aerodynamic force, so that only inertial forces are isolated. In terms of the experiment, it is $\vec{F}_{empty,f} - \vec{F}_{empty,f_{static}}$.

In terms of the experiments, the aerodynamic force is:

$$\vec{F}_{aero} = \vec{F}_{U_\infty,f} - \vec{F}_{V_0,f_{static}} - (\vec{F}_{empty,f} - \vec{F}_{empty,f_{static}}) \tag{4.3}$$

The forces obtained during the four separate experiments must go through a post-processing phase to clean up the signal and adequately represent the results.

4.2 Post-processing

The post processing procedure of the force data is relatively straightforward. Naturally, it is heavily dependent on the manner in which the results need to be represented.

This post processing phase has a double objective: First, to take the raw input signals taken from the F/T sensor and filter out noise as much as possible, as well as doing a mean of all the captured cycles over a single cycle. Second, to show the result in a coherent and adequate manner, to best analyze the results and draw the appropriate conclusions.

To achieve this double objective, a Matlab script has been developed. The program takes as input the fundamental experiment parameters, and outputs the necessary plots. These

parameters are fluid density, ρ, free stream velocity, U_∞, wing oscillation frequency, f, and wing surface area S.

4.2.1 Mean Cycle Computation

To achieve a result as accurate as possible, the data is captured over several cycles, and the mean forces over the cycle are computed.

To perform this operation, it is first necessary to compute the total number of cycles n, in a captured data set. The number of cycles is a function of data points captured, airfoil flapping frequency and sampling frequency, f_s.

$$n = datapoints \cdot \frac{f}{f_s} \tag{4.4}$$

Once the number of cycles is computed, it is possible to reshape the raw data set into a single mean cycle.

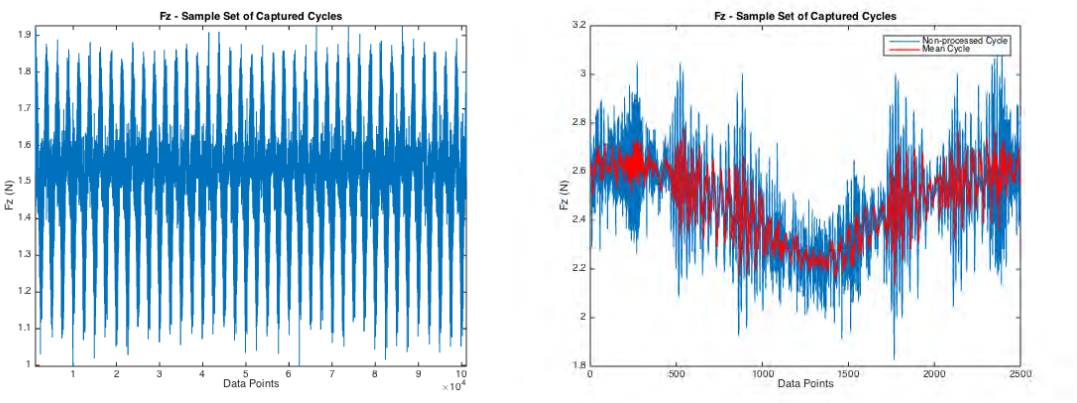

(a) **(b)**

FIGURE 4.1: A representation of several captured cycles of F_z (a), and the mean cycle (b), with a comparison of pre and post reshape.

As can be seen in figure 4.1, the reshape and mean cycle calculation process renders a new curve, in red, slightly less noisy that the non-processed data, in blue. The figure shows the procedure for an $f_s = 1000$ Hz, with F_z in N in the y-axis, and data points in the x-axis (2500 data points/cycle).

This process must be performed to the data of each of the four previously described experiments, and to each of the x,y and z components.

4.2.2 Noise Filter

Even after computing the mean cycle, the signal is much too noisy for analysis. To filter out the high frequency noise produced by the hydrodynamic tunnel pumps and the wing motion actuators, a low-pass filter is useful.

A low-pass filter is a filter that passes signals with a frequency lower than the designed cutoff frequency, and attenuates the signals that are higher than the cutoff frequency.

A Butterworth filter is a good option for the purposes of this project. To design the filter, it is necessary to set a normalized cutoff frequency, expressed as:

$$\omega_n = \frac{2f_c}{f_s} \tag{4.5}$$

where f_c is the cutoff frequency and f_s the sampling frequency. Applied to the same sample as in figure 4.1, the output of the filter is:

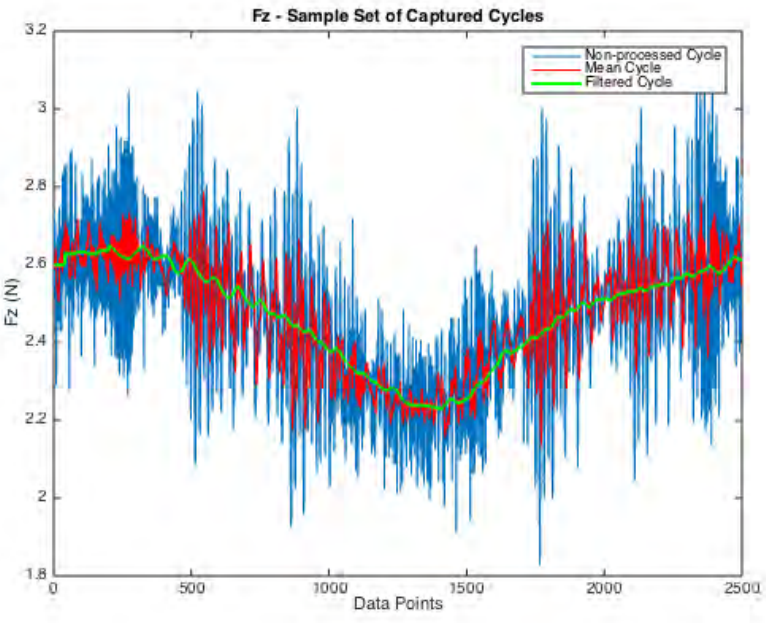

FIGURE 4.2: Visual comparison of the three stages of the signal filtering process. This is for a cutoff frequency of 10 Hz.

More than one filter may be necessary to achieve better results. A bandstop Butterworth filter may also prove useful. This filter attenuates signals within a range of frequencies.

Again, this filter must be applied to each of the axial forces of each of the four experiments.

4.2.3 Aerodynamic Force Isolation

The result of applying the previous steps to the data gathered from the four experiments is the force data necessary for isolating the aerodynamic force, over a single cycle and with noise reduction.

As explained in section 4.1, we have that:

$$\vec{F}_{aero} = \vec{F}_{U_\infty,f} - \vec{F}_{V_0,f_{static}} - (\vec{F}_{empty,f} - \vec{F}_{empty,f_{static}}) = \vec{F}_{tot} - \vec{F}_{buoy} - \vec{F}_{mass} - \vec{F}_{inertial} \tag{4.6}$$

The F/T sensor is attached to the wing. Therefore, the isolated aerodynamic forces are in body axes, F_{X_B},F_{Y_B}, and F_{Z_B}

4.2.4 Frame of Reference Transformation

In order to study the resulting forces, the most useful reference frame is an outer coordinate system aligned with the hydrodynamic tunnel. In this frame of reference, lift and thrust forces can easily be identified and represented. However, the aerodynamic forces are measured using an F/T sensor attached to the moving wing. Therefore, some transformations are necessary.

First, it is important to understand the axis convention of the force/torque sensor. For this model, a quick look at the manual [27] shows the z-axis goes in the direction of the cable. The x-axis is indicated by a notch in the device, and the y-axis is naturally orthogonal to both. The positive orientations are indicated in figure 4.3.

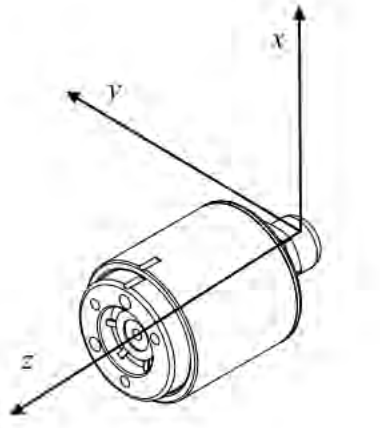

FIGURE 4.3: Schematic of the F/T sensor with appropriate axis.

The forces of interest for this particular 2D project, where 3D effects are not accounted for, are the force normal to the airfoil, and the force in the chordwise (axial) direction, shown in figure 4.4 as N, and A, respectively. The new coordinate system, with x in the direction of U_∞ and z in the up direction can also be seen.

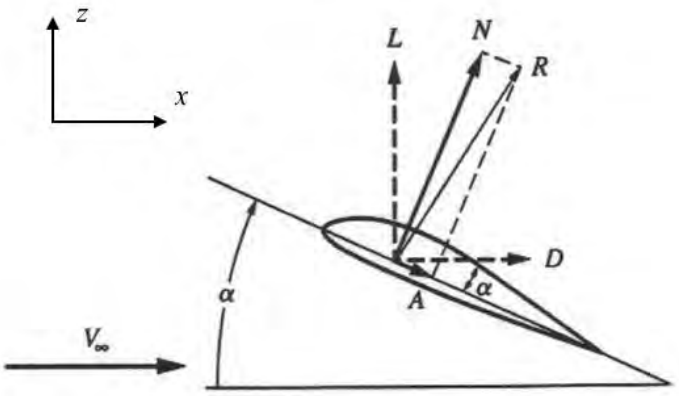

FIGURE 4.4: Schematic of the airfoil within the hydrodynamic tunnel. The problem is reduced to this 2D plane. Image modified from a sample in www.aerospaceweb.org

The sensor is attached to the wing in such a way that chordwise force, $F_{X_B} = -A$ and normal force, $F_{Z_B} = -N$. Therefore it is necessary to change the signs of both.

The next transformation is to change from body axis, x_B,z_B to the new x, z frame of reference. The objective of this transformation is to obtain L and D as in figure 4.4. Knowing the geometric angle of attack of the airfoil, the transformation is as follows:

$$\vec{z} = \vec{z}_B \cdot cos(\theta(t)) - \vec{x}_B \cdot sin(\theta(t)) \tag{4.7}$$

$$\vec{x} = \vec{z}_B \cdot sin(\theta(t)) + \vec{x}_B \cdot cos(\theta(t)) \tag{4.8}$$

Figure 4.5 provides a sketch of the operation.

4.2.5 Force Coefficient Computation

Once the aerodynamic forces are computed, with the transformations described in the previous section, computing the final forces and coefficients is straightforward.

$$L = F_{Z_B} \cdot cos(\theta(t)) - F_{X_B} \cdot sin(\theta(t)) \tag{4.9}$$

$$D = F_{Z_B} \cdot sin(\theta(t)) + F_{X_B} \cdot cos(\theta(t)) \tag{4.10}$$

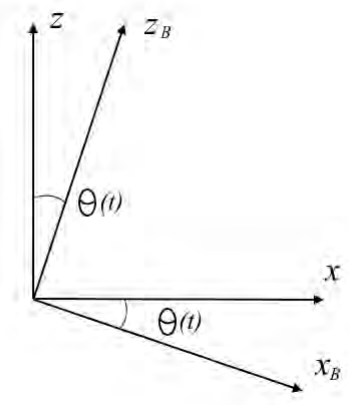

FIGURE 4.5: Transformation from body axis to fixed reference frame.

Finally, to compute the lift and drag coefficients, non-dimensionalizing the forces with dynamic pressure is required:

$$C_L = \frac{L}{\frac{1}{2}\rho S V^2} \tag{4.11}$$

$$C_D = \frac{D}{\frac{1}{2}\rho S V^2} \tag{4.12}$$

where ρ is fluid density, S airfoil surface area, and $V = U_\infty$ velocity of the fluid. Since this experiment is centered on studying thrust evolution, it is a good idea to define a thrust coefficient, which can easily be done from C_D:

$$C_T = -C_D = \frac{T}{\frac{1}{2}\rho S V^2} \tag{4.13}$$

Chapter 5

PIV Processing

In chapter 3, the PIV system was described, and it components explained. Once the images have been captured, they need to be processed. This chapter describes the transformation process of the raw images to a quantitative and qualitative visualization of the flow.

5.1 Cycle Discretization

One very important parameter to choose for the experiment is the frequency of image capture performed by the camera, f_{cam}. This parameter is going to determine the number of phases per cycle, n_ϕ that is going to be acquired. In a sense, this n_ϕ determines the framerate or resolution of the cycle animation. A very low number does not require many image captures, but will result in a poor animation. If the number is too high, the number of images must be very large to capture a sufficient number of equal phases for a good mean. It is also limited by the capture frequency of the camera, f_{cam}, which is limited to 30 Hz.

Fortunately, there is a workaround the maximum f_{cam}. It is possible to capture different phases at different cycles, instead of capturing the same phases each cycle. A lower capture frequency that does not render a whole number of phases per cycle, can be selected, and the data captured over n cycles until the number of phases becomes whole. In that manner, a higher number of unique, equally spaced phases is achieved, without maximizing f_{cam}. Only a longer capture time is required.

Let us take a look at a quick example. Let us assume an $f = 1Hz$. On figure 5.1, the left image shows what would occur with an $f_{cam} = 4Hz$. Four phase points are captured over a single cycle. If however f_{cam} is increased to 4.5Hz, 4.5 phases would be

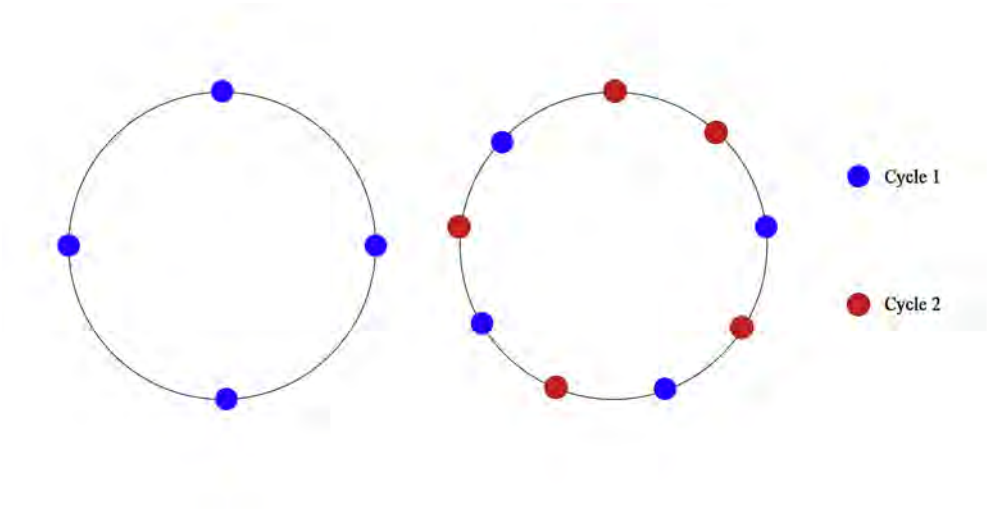

FIGURE 5.1: Cycles manipulation to maximize phase points captured without reaching f_{cam} limits.

captured per cycle. That means over 2 cycles 9 equally spaced phase points are obtained, rendering a much higher resolution result without breaking the limits of the camera.

5.2 Image Processing

In order to obtain a final velocity field, the images obtained through the laser and camera systems must be processed and transformed into qualitative information. That is, the image pairs must be processed in order to obtain vectors.

This is usually performed with specialized software that reads the images and uses a correlation method to determine particle pairs and draw the final vector. To do this, each image pair is divided into so called interrogation windows. Corresponding windows for both frames are compared to search for particle pairs. A correlation method, such as Fast Fourier Transforms (FFT) will show the maximum-probability pairs. With these pairs, vectors can be constructed. More complex mechanics, such as outlier detection (and substitution for an average of the neighboring vectors) and factoring for particles that move from one interrogation window to the other can be implemented.

Often, this process is done iteratively, reducing the interrogation window size and increasing the velocity field resolution.

It is also common to run the results through some form of post-processing, to remove outliers, clean up the data, remove noise and display the data in a more meaningful way.

For this particular experiment, a custom software written by Professor Tommaso Astarita and Dr. Stefano Discetti was utilized. The initial interrogation window is 64x64

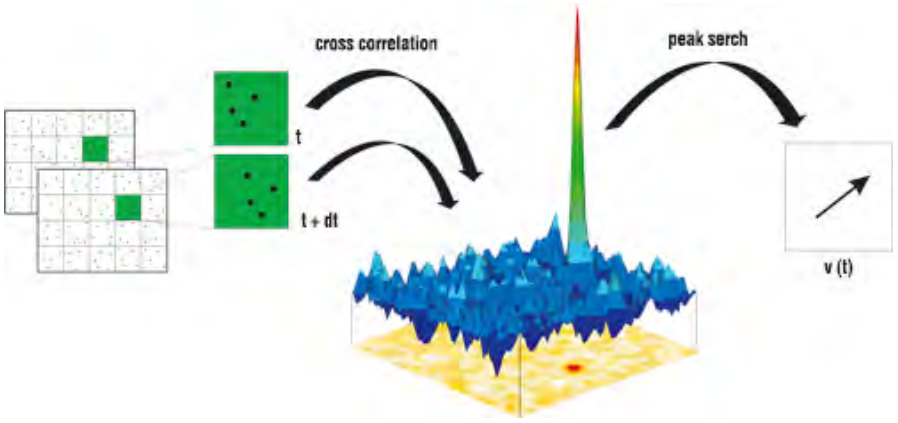

FIGURE 5.2: Image evaluation process in PIV. FFT peak correlation. Image from Dantec Dynamics.

pixels, and the final one is 32x32, rendering quite a high-resolution velocity field, with each window being just over 3x3mm.

5.3 Post-processing

The post processing of the PIV results is a thorough process, as the raw data is not optimal. Once the previously mentioned custom written software has processed the images, a set of files (one per image-pair), is generated. These files contain information regarding velocity in the x-direction (U), velocity in the y-direction (V), and the x and y positions of these velocity vectors (X, and Y, respectively). That is, a velocity field per image pair.

This files need to be passed through a series of filters to represent the results in their optimal format.

5.3.1 Re-ordering the Files and Obtaining Phase Mean

To perform this operation, a Matlab program was written, that takes the total number of velocity fields obtained, the frequency of the motion of the wing, f, and the capturing frequency of the camera system, f_{cam}. This program then outputs data files with the mean velocity vectors ($\overline{U}$,$\overline{V}$) and their positions ($\overline{X}$,$\overline{Y}$).

The manner in which the program works is as follows:

First, with the frequency of motion of the wing (f), and the capture frequency of the camera system (f_{cam}) it computes the total number of phase points per cycle (n_ϕ) acquired. As explained before, to work around the maximum f_{cam}, this must be a whole

number, so it is multiplied by a factor n until it is achieved. This factor n is the number of cycles that need to be ran in order to acquire n_ϕ number of phase points per cycle.

$$n_\phi = n \cdot f_{cam} \cdot T = n \cdot f_{cam} \cdot (\frac{1}{f}) \tag{5.1}$$

Then, with the total number of snapshots acquired, which naturally is always a multiple of n_ϕ, it is then possible to compute the total number of images for each *unique* phase captured, which may be called n_{images}. This is a simple division: $n_{images} = snapshots/n_\phi$.

Finally, the program makes a double iteration, to both compute the phase mean, and order the images correctly.

To perform the first operation, it iterates over n_ϕ, so that the operation is performed for each of the unique captured phases of the cycle. For each of these iterations, it iterates once more, this time over n_{images}, so that for each phase, it associates all of its images.

Now, within this second loop, each of the velocity fields is read, and data extracted. For each associated velocity field, the program extracts an X,Y grid, horizontal velocity , U, vertical velocity, V, and a correlation factor, to determine the areas where correlation was best, and where it was poor. This method makes it possible to later represent the data in many different ways.

Each time the second loop is exited, the script executes two important actions. First computing a phase mean, which is trivial. Then ordering the images. This task is relatively simple. Knowing the position of each image, which corresponds to its index within the first loop, it is possible to compute the time at which the image was captured.

$$t = \frac{index}{f_{cam}} \tag{5.2}$$

With this information, it is possible to compute which of the n cycles the phase belongs to, and then establish its value:

$$n = ceil(t/T) \tag{5.3}$$

$$\phi_{cycle} = \frac{t - (T \cdot (n-1))}{T} \tag{5.4}$$

The output of the program is a file per n_ϕ, containing the phase mean of X,Y,U,V, and correlation factor. This data will later be used for generating representations and analyzing results.

5.3.2 Non-Dimensionalization

The data obtained through the previously defined process is not in a usable unit. Because it is extracted from an image file, pixels are the defining unit.

To obtain a conversion factor, it is necessary to analyze some sample images and extract a value from a know measure. To perform this operation, Gimp, an open source image processing software was utilized.

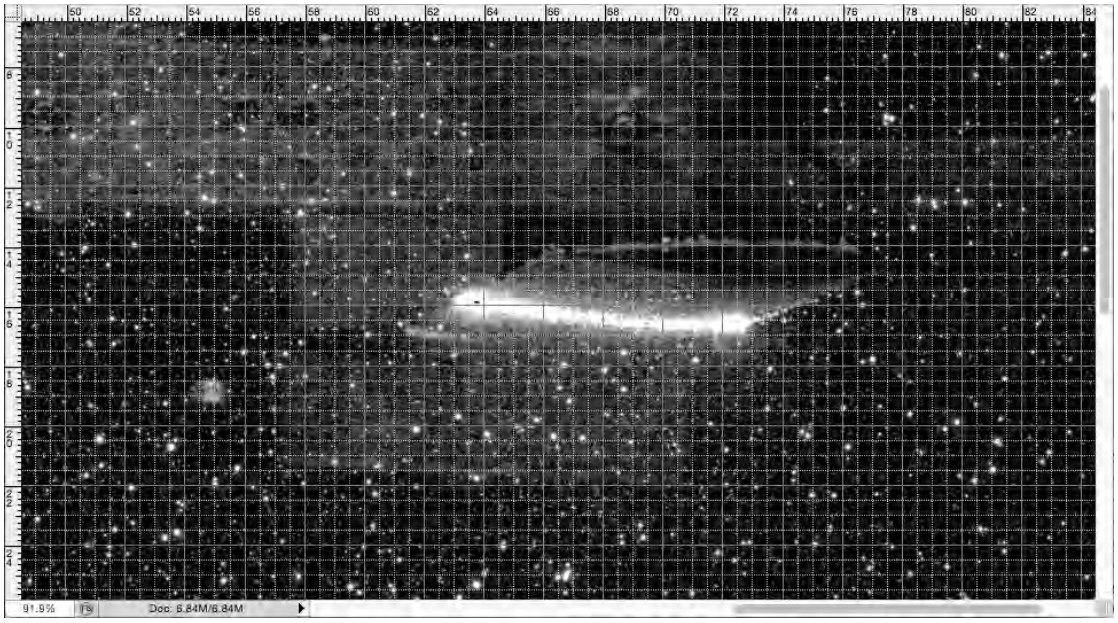

FIGURE 5.3: Analyzing the images to obtain a conversion factor, and establish an origin point.

Knowing the chord of the wing, and measuring the pixels in the photo, obtaining a conversion factor is simple. For this particular setup, it works out to 10.25 px/mm. At this point, it is also useful to determine what will be considered the origin point. A useful point is the $c/4$ point for an X origin, the pivoting point of the wing, and the axis of symmetry of the wing when $\phi = 0$, for Y origin.

Once the data is in physical units, it is possible to non-dimensionalize it. Units of length are non-dimensionalized with the chord of the wing, c, and velocity with the free stream velocity, U_∞.

Also worth mentioning, is that raw U and V data are output as length units. To obtain velocity, it is necessary to divide by the time lapse between laser pulses, dt.

5.3.3 Shadow Removal

The laser is placed under the wing to illuminate the particles. The positioning of the laser generates a shadow, where seeding particles cannot be illuminated, and therefore no data is obtained for that section. This phenomenon is illustrated in figure 5.4, with the low correlation area circled in red. A more advanced lighting system from multiple angles may solve this issue.

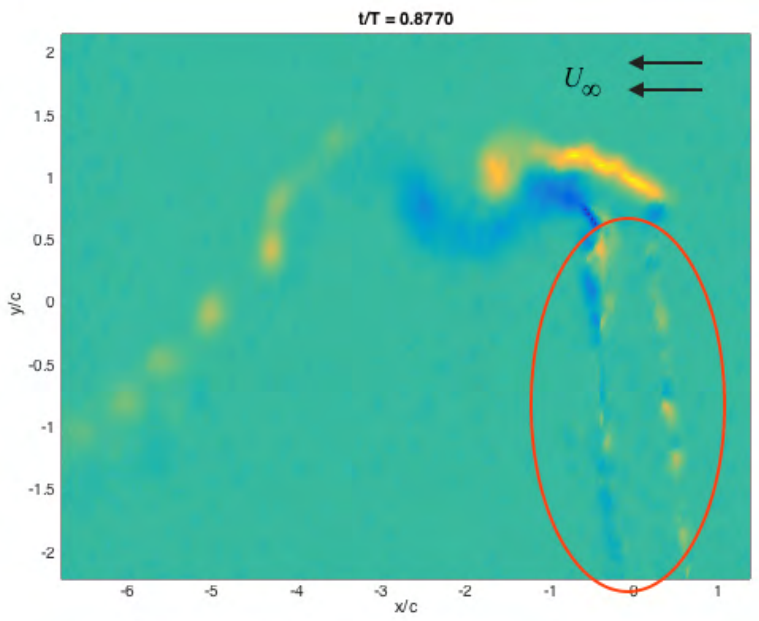

FIGURE 5.4: Shadow producing erroneous results in the PIV visualization.

To remove the shadow, different processes must be followed, depending on the symmetry of the motion of the wing, and that of the airfoil. Nonetheless, the initial step is common to both.

The first step is the blanking of the shadow. This process relies on one of the values saved in the output files of the PIV software. The correlation factor helps determine which points displayed are not particularly well correlated. The density of low correlation points is especially high in the area of the shadow. By carefully choosing a limit for allowed correlation factor, it is possible to fully blank the shadow in each frame of the cycle.

Choosing a correct value or limiting the affected area is important to avoid removing useful information, such as the spots seen at the bottom left of figure 5.5.

Now, the blanked space needs to be filled with the corresponding flow. This procedure differs for symmetric and non symmetric airfoils and oscillation. For symmetric airfoils with a symmetric oscillation, it can be assumed that the flow in the upper region of the

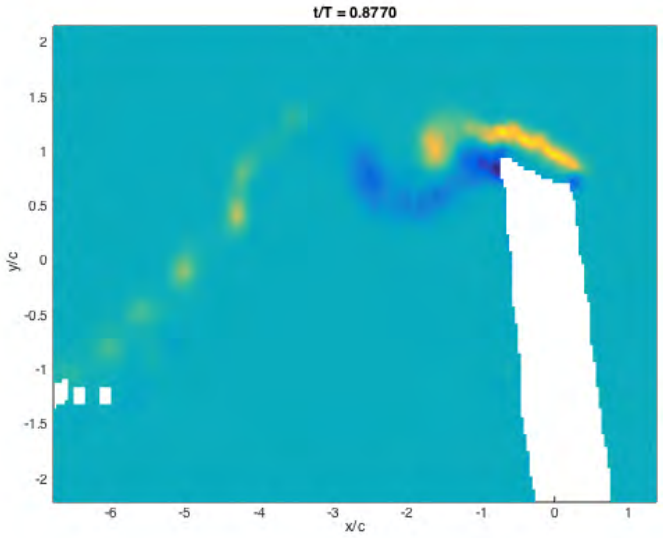

FIGURE 5.5: Fully blanked shadow by using the correlation factor. Choosing a correct value or limiting the affected area is important.

airfoil is identical to the flow in the lower region of the airfoil with a phase difference of 180°, that is, a difference of $t/T = 0.5$ with respect to the time of the cycle.

It is possible that some issues arise in this process. If the case is not well discretized, or if more accurate results are desired, it may occur that the phases acquired do not have an equivalent with a 180° phase shift. If this occurs, an interpolation is necessary to acquire the missing phases. A simple linear interpolation is an option: to obtain a phase at any point between two acquired phases, a weighted average of the velocity fields U,V, and the correlation factor renders sufficiently accurate results. For a cycle with data every n degrees, simply:

$$U_{n+x} = U_0\left(\frac{n-x}{n}\right) + U_{0+n}\left(\frac{x}{n}\right) \tag{5.5}$$

where x is phase desired, and U_0,U_{0+n} the velocity fields for two phases given.

After interpolation is complete and the data for the captured phases and their 180° shift is successful, it is necessary to place the lower region missing data over the shadow blanking. For this operation, it is necessary to track the position of the wing for each of the frames. Then, each corresponding phase shift must be flipped vertically around the horizontal axis, so that the information of the lower region of the wing can be placed.

In figure 5.6, the transparency of the images has been modified to easily view the process on the left. It is possible to see the flow in the lower region of the wing is now visible over the shadow. The image on the right shows the final product.

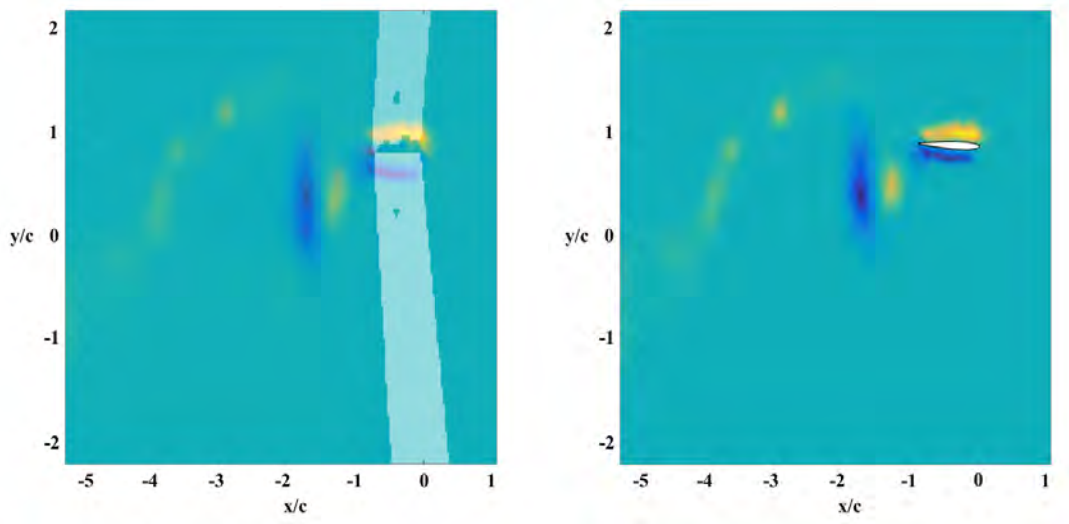

(a) **(b)**

FIGURE 5.6: The process with lowered transparency, to clearly see both images (a), and (b), the cleaned up image to see the final product for one frame.

Asymmetric oscillations are slightly more complicated. Although the processing and shadow blanking is essentially the same, and can be performed with the same software, the experimental procedure changes. For these motions, the flow in the upper and lower region do not have an analogous with a $t/T = 0.5$ shift. In order to obtain this data, it is necessary to perform an identical experiment with opposing kinematics.

5.3.4 Other Display Options

One of the main objectives of the project is understanding the evolution of the vortical structures that form in the flow, and how they affect force coefficients. Thus, visualizing the vorticity is useful.

Vorticity, $\vec{\omega}$ is the curl of the velocity field, and serves as a measure of the local rotation of the fluid.

$$\vec{\omega} = \nabla \times \vec{U} \tag{5.6}$$

In 2D problems such as this one, it can be expressed as:

$$\vec{\omega} = \left(\frac{\delta u_y}{\delta x} - \frac{\delta u_x}{\delta y}\right) \cdot \vec{z} \tag{5.7}$$

where x and y are horizontal and vertical components, respectively. Vorticity is non-dimensionalized with c/U_∞.

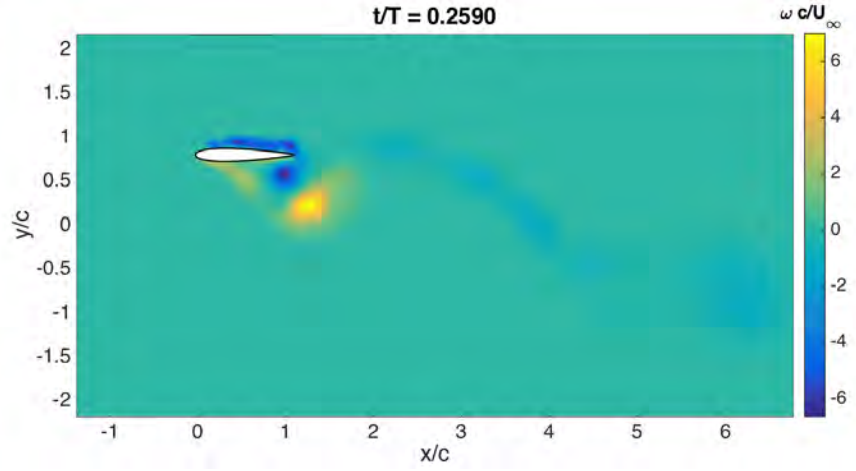

FIGURE 5.7: Vorticity visualization is useful for studying the vortical structures.

Chapter 6

Force Measurements: Results

In this chapter, the force results of the different cases that were ran at the water channel will be analyzed. In addition, the experimental conditions will be clearly defined for each case.

6.1 Experimental Conditions

A total of 6 cases were studied for this project. These cases varied in mean pitch angle, θ_m and pitch amplitude, θ_0, with the objective of identifying the best geometric angle of attack evolution for higher lift and thrust production. Table 6.1 summarizes the conditions for the 6 cases.

Case	θ_0	θ_m	*Parameter*	*Value*
$C1_{PP,0}$	0°	0°	f:	0.4 Hz
$C2_{PP,10}$	0°	10°	ϕ:	90°
$C3_{MF,0}$	10°	0°	U_∞:	0.12 m/s
$C4_{MF,10}$	10°	10°	Re:	3600
$C5_{HF,0}$	20°	0°	St:	0.2
$C6_{HF,10}$	20°	10°	k:	0.1π

TABLE 6.1: Conditions of the 6 experimental cases.

As can be seen, there are three different pitch amplitude conditions: Pure plunge ($\theta_0 = 0°$), moderate flapping ($\theta_0 = 10°$) and heavy flapping ($\theta_0 = 20°$). For each of theses cases there are two conditions: null mean pitch, and 10° of mean pitch angle. The phase lag between pitching and plunging motions, ϕ, is set to 90°. See equation 2.2

The values of these pitching conditions were chosen to obtain a large enough field of results, without compromising the limits of the motion system actuators.

6.1.1 Governing Parameter Selection

Table 6.1 shows no variation of the three governing parameters of the flapping wing problem. These parameters were selected for varying reasons:

i. The Reynolds number was set to 3600. To achieve this Re, U_∞ was set to 0.12 m/s. This value is the lowest that can be handled given the balance sensitivity.

ii. Strouhal number was selected to match that of typical biological flyers. In nature $St = 0.2$ is a common value, and it is suspected to be adequate to maximize aerodynamic lift and thrust. To keep this value with $U_\infty = 0.12$ m/s, the oscillation frequency, f was set to 0.4 Hz.

iii. Reduced frequency was then, $k = 0.1\pi$. This is the result of setting $Re = 3600$ and $St = 0.2$, and consequently $U_\infty = 0.12$ m/s and $f = 0.4Hz$.

As a side note, f_{static}, to capture the static data necessary to compute the forces, as explained in 4.1, was set to $1/10^{th}$ of f, that is, $f_{static} = 0.04\ Hz$

6.1.2 Wing Geometry

Of course, the geometric characteristics of the experiment were fixed for all cases.

Profile Geometry	NACA 0012
Plunge Amplitude, h_0	30 mm
Airfoil Chord, c	30 mm
Wing Span, b	490 mm
Pivot Point, x_p/c	0.25

TABLE 6.2: Geometric characteristics of the wing.

6.2 Lift and Thrust Coefficient Evolution over Time

One of the more interesting analysis that can be performed on the results is a look at the evolution of the force coefficients over the length of the cycle. In this manner, it is possible to see exactly what is ocurring at each point in time of the cycle, non-dimensionalized with the period, T.

For each of the figures, C_L, on the left, and $C_T = -C_D$, on the right, are represented. In addition, the upstroke and downstroke periods of the cycle are differentiated with colors, for a richer analysis. In red, downstroke motion, in blue, upstroke.

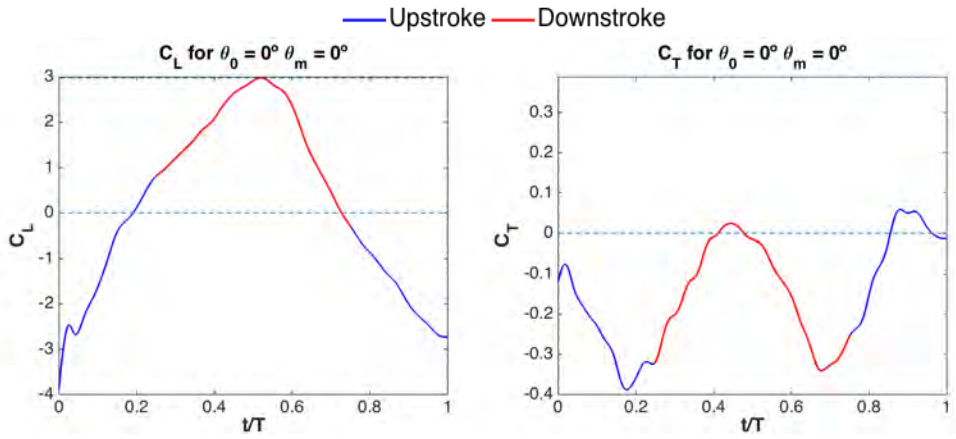

FIGURE 6.1: Evolution of aerodynamic force coefficients over a single cycle for case $C1_{PP,0}$ ($Re = 3600$, $St = 0.2$). On the left, C_L, and the right C_T for $\theta_0 = 0°$ and $\theta_m = 0°$

The case of pure plunge and 0 mean angle of attack, a perfectly symmetric motion, should display a symmetric distribution of lift. However in 6.1, we can see that this is not entirely the case. While some of the inaccuracies, such as the downward peak to the left of the image are due to the signal filter, it is clear that the upstroke and downstroke motions are not perfectly symmetric: they should be separated at exactly the $C_L = 0$ reference line. A possible explanation is the strong vortical structures at the transition point, which affect lift. They will be studied later. Nonetheless, the peaks are reasonably distributed. The positive peak in the middle of the downstroke, and the negative peak in the middle of the upstroke. Value wise, they are also quite similar, approximating an absolute value of three for both instances, ignoring filter inaccuracies. This is reasonable, as the distribution of α_e is equal but opposing in sign.

In general, we should expect C_T results to be less accurate than C_L results. This is due to the scale of the values measured, C_T being a smaller scale, thereby more affected by noise and equipment error. For this case ($\theta_0 = 0°$, $\theta_m = 0°$), there are two differentiated positive peaks, at approximately $t/T = 0.25$ and $t/T = 0.75$ both just breaking into thrust production. These points coincide with the transition points from upstroke to downstroke and vice versa.

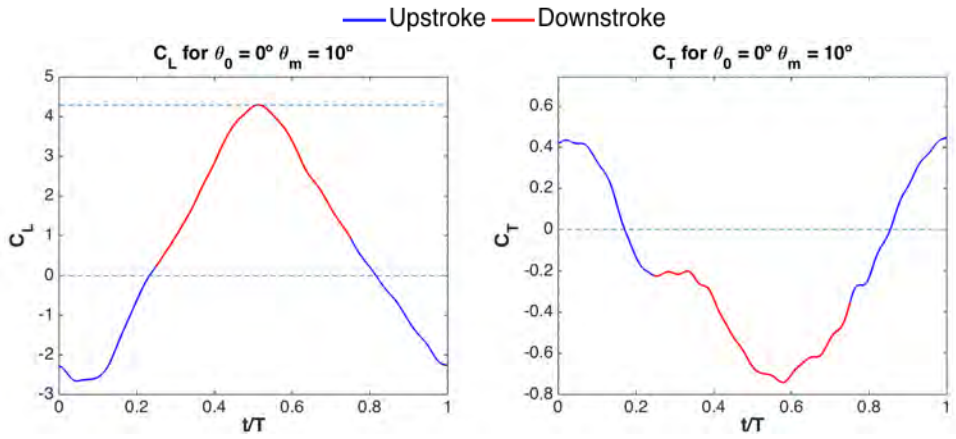

FIGURE 6.2: Evolution of aerodynamic force coefficients over a single cycle for $C2_{PP,10}$ ($Re = 3600$, $St = 0.2$). On the left, C_L, and the right C_T for $\theta_0 = 0°$ and $\theta_m = 10°$

Figure 6.2 is a good example to study the effects of adding a θ_m to the motion. Looking at equation 2.4, it is easy to deduce that adding a mean angle of attack essentially shifts upward the α_e curve. This effect is illustrated in figure 6.3 This upward shift causes an overall increase in lift production, in both upward and downward strokes. The peak distribution is then maintained, with the positive peak at $t/T = 0.5$ and the negative peak at around $t/T = 0 = 1$, but the peak values are clearly higher.

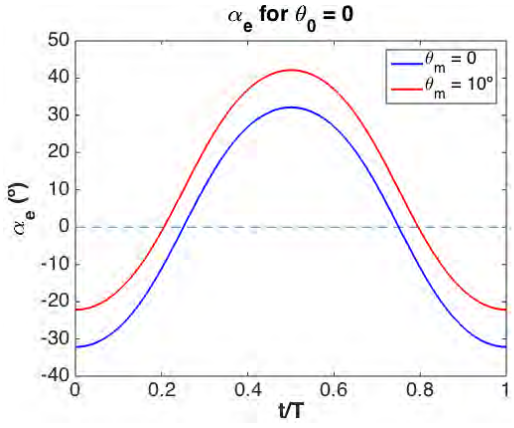

FIGURE 6.3: For pure plunge, the effect on α_e of adding a $\theta_m = 10°$. The shift is clearly visible.

As for C_T, the effect of adding a mean angle of attack is of an overall reduction in thrust. To understand what is happening, it is useful to analyze the forces from a normal and axial force perspective: Normal force acting on the plate can be considered the dominating load. The horizontal projection of this force is the thrust/drag component. For growing effective angles of attack, normal force component projects increasingly backwards, increasing drag. In other words, thrust decreases as α_e increases. Contrasting figures 6.2 and 6.3, it is clear that the theory holds. An interesting effect occurs at

the transition from upstroke to downstroke, at $t/T = 0.25$. The rate of decrease of C_T slows down. Looking at figure 6.3, it is possible to see that this slow-down corresponds with an inflection point in the plot. During the transition, strong vortices are generated, which likely influence the direction of the force, causing this effect. This is a relatively simplified explanation, as it does not account for induced flow effects of the wake.

Because α_e has been shifted up, higher angles of attack in absolute value will be seen in downstroke than upstroke. Thus, negative C_T peak is larger than the positive peak in absolute value.

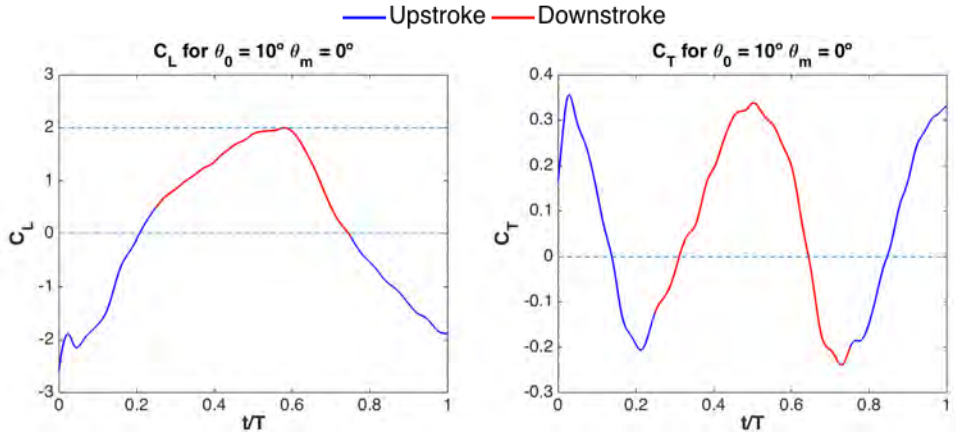

FIGURE 6.4: Evolution of aerodynamic force coefficients over a single cycle for $C3_{MF,0}(Re = 3600,\ St = 0.2)$. On the left, C_L, and the right C_T for $\theta_0 = 10°$ and $\theta_m = 0°$

Moving towards cases with pitching amplitude, it is possible to start noticing certain trends. For example, it appears that cases with $\theta_m = 0°$ show wider peaks in the C_L distribution, and cases with $\theta_m = 10°$ show thinner, more defined positive peaks, but wider lower peaks.

For $C3_{MF,0}$, seen in figure 6.4, one can notice that although there is now a pitching amplitude, the peaks are still very similar in absolute value. This is reasonable, as α_e history is still symmetric as there is no θ_m, and so the mean C_L of the cycle should approach 0.

The evolution of thrust over the period of the cycle shows similarities with $C1_{PP,0}$: the dragging peaks are placed at the transition from upstroke to downstroke and vice versa, and the thrust producing peaks in the middle of the strokes. Cases with $\theta_m = 0°$ are the only promising cases in terms of thrust production.

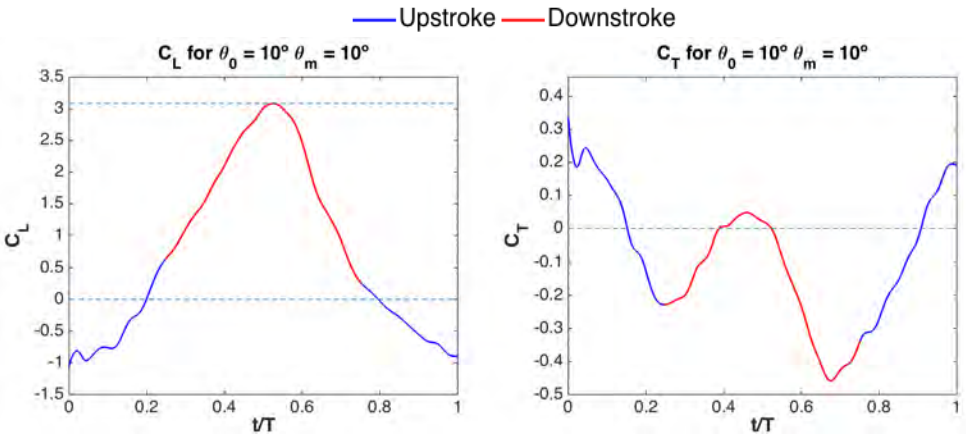

FIGURE 6.5: Evolution of aerodynamic force coefficients over a single cycle for $C4_{MF,10}$ ($Re = 3600$, $St = 0.2$). On the left, C_L, and the right C_T for $\theta_0 = 10°$ and $\theta_m = 10°$

Regarding C_L, looking at $C4_{MF,10}$, it again appears that the distributions are dominated by θ_m. Thus, it is possible to see similar results in evolution over t/T than its pure plunge analogous, $C2_{PP,10}$. However, there are some crucial differences. Figure 6.5 displays a positive peak in C_L lower than in the pure plunge case. Nonetheless, the negative peak is noticeably smaller in absolute value as well, so a higher mean C_L may be expected. The lower values of C_L are explained looking at the α_e evolution in figure 6.6.

In terms of C_T, the results are quite interesting. It is easy to see that values at transition points are the same in $C2_{PP,10}$ and $C4_{MF,10}$. However, drag peaks are much lower in $C4_{MF,10}$, and thrust peaks only slightly lower, rendering a quite lower overall cycle drag. A look at the effective angle of attack histories for both cycles sheds some light on this phenomenon: at the transition points, a_e values are equal, but in the middle of the strokes, much lower in absolute value in $C4_{MF,10}$.

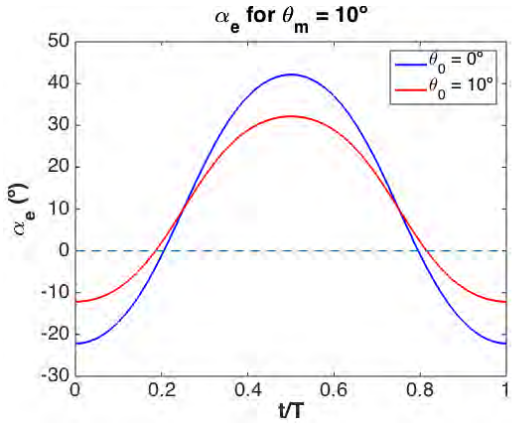

FIGURE 6.6: Comparison of α_e evolution for $\theta_m = 10°$.

Heavy flapping cases follow the same trends as moderate flapping cases.

In case $C5_{HF,0}$, seen in figure 6.7, equal C_L peak values in absolute value with close to null mean C_L, and promising results in terms of thrust generation.

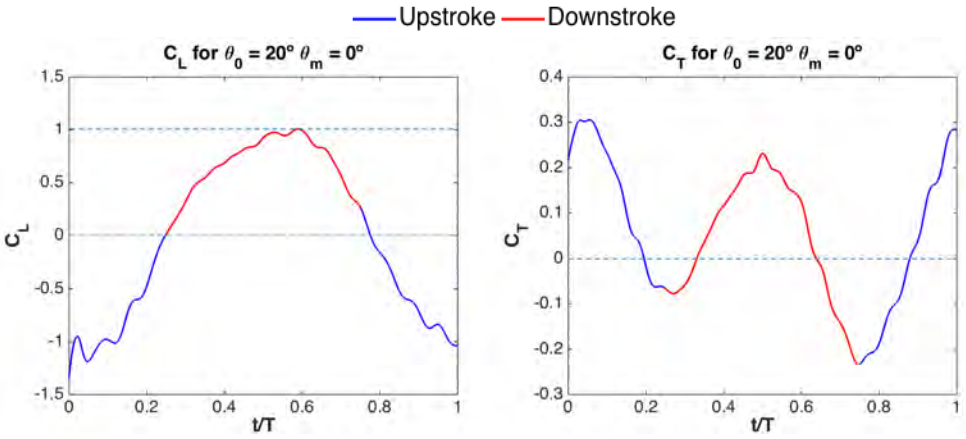

FIGURE 6.7: Evolution of aerodynamic force coefficients over a single cycle for $C5_{HF,0}$ ($Re = 3600$, $St = 0.2$). On the left, C_L, and the right C_T for $\theta_0 = 20°$ and $\theta_m = 0°$

In case $C6_{HF,10}$, seen in figure 6.8 high C_L peak value, although lower than $C4_{MF,10}$, and more drag than thrust.

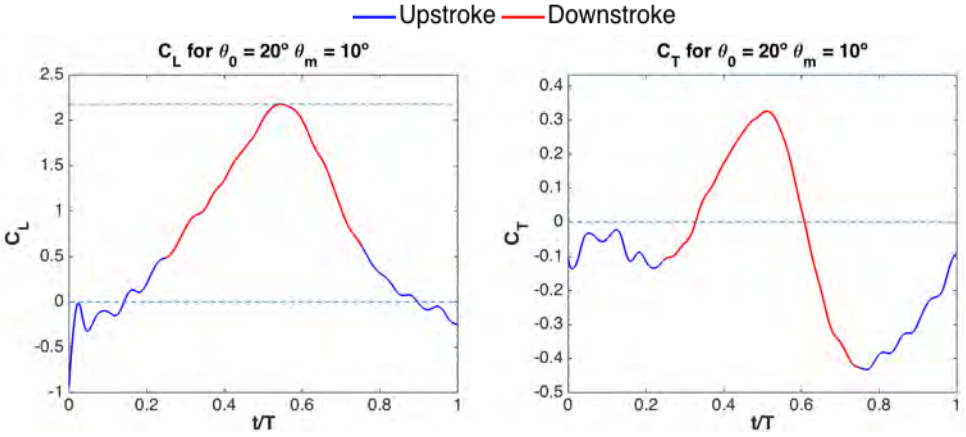

FIGURE 6.8: Evolution of aerodynamic force coefficients over a single cycle for $C6_{HF,10}$ ($Re = 3600$, $St = 0.2$). On the left, C_L, and the right C_T for $\theta_0 = 20°$ and $\theta_m = 10°$

These explanations are based solely on the data that can be extracted from these plots and α_e histories. Some effects can only be explained by looking at the evolution of the vortical structures developed in the flow. For more in depth explanations of the phenomena seen in the graphs, PIV analysis is necessary, and will be covered in Chapter 7.

6.3 Mean Lift and Thrust Coefficient as a function of Angle Kinematics

Determining mean force coefficient values can be a useful tool in determining the best configurations for lift or thrust production. During the period of oscillation, lift and thrust will experience changes in sign, meaning at some points of the motion the airfoil may be producing lift or thrust, and in a different point it may be producing a detrimental lifting force or drag. By finding the mean, it is possible to obtain the overall result of the cycle. A positive $\overline{C_L}$ indicates a lift producing configuration, and a positive $\overline{C_T}$ a thrust producing motion.

Any time a mean value is computed, determining how much the members of a group differ from the mean value for the group is important. An interesting quality to study is thus the standard deviation, σ, as it helps visualize the variability of the force coefficients within the cycle. For example, if within the cycle the forces are relatively constant, a low σ would be expected. If however the peaks are far apart, a higher σ would be the norm. It is defined as:

$$\sigma_{C_X} = \sqrt{\frac{1}{N}\sum_{i=1}^{N}(C_X(i) - \overline{C_X})^2} \tag{6.1}$$

where C_X is C_L or C_T, and N the number of data points for each cycle. Table 6.3 contains a summary of each of the ran cases and their resultant $\overline{C_L}$ and $\overline{C_D}$, as well as their standard deviations.

Case	θ_0	θ_m	$\overline{C_L}$	$\overline{C_T}$	σ_{C_L}	σ_{C_T}
$C1_{PP,0}$	0°	0°	0.1961	-0.1467	1.8668	0.1332
$C2_{PP,10}$	0°	10°	0.6683	-0.1777	2.2447	0.3808
$C3_{MF,0}$	10°	0°	0.0941	0.0792	1.3674	0.1919
$C4_{MF,10}$	10°	10°	0.7318	-0.0894	1.3291	0.1913
$C5_{HF,0}$	20°	0°	0.0119	0.0594	0.7444	0.1516
$C4_{HF,10}$	20°	10°	0.7384	-0.0848	0.7997	0.2185

TABLE 6.3: $\overline{C_L}$ and $\overline{C_T}$ for each of the experimental cases ($Re = 3600$, $St = 0.2$).

Figure 6.9 is a visualization of the values of this table, plotted for fixed θ_m. In red, $\theta_m = 10°$, in blue $\theta_m = 0°$. The force coefficient values are therefore displayed as a function of θ_0.

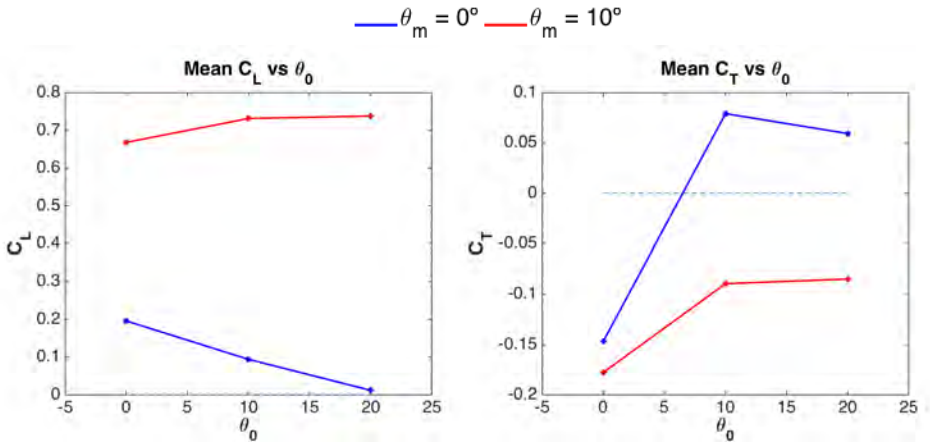

FIGURE 6.9: On the right, $\overline{C_L}$, on the left $\overline{C_D}$ as a function of θ_0 for $\theta_m = 0°$,$\theta_m = 10°$ ($Re = 3600$, $St = 0.2$)

Concerning C_L, being a symmetric airfoil, cases with $\theta_m = 0°$ should render a null coefficient. This is because the upstroke and down stroke motions are identical but in opposing direction, and should therefore exhibit opposing effective angles of attack, cancelling each other out. While this seems to hold true for $\theta_0 = 20°$, it does not hold true for $\theta_0 = 0°$, $\theta_0 = 10°$. Instead, it seems to follow a linear pattern, with slope -0.2π. The error is maximum where σ_{C_L} is maximum, and corresponds to about 7%, which is reasonable given the noise conditions. In the case of $\theta_m = 10°$, there is obviously a positive shift in C_L, as the airfoil now has a mean angle of attack, effectively shifting up α_e. Also noticeable is a positive correlation between higher pitch amplitude and C_L. The change is much more noticeable from $\theta_0 = 0°$ to $\theta_0 = 10°$ than from $\theta_0 = 10°$ to $\theta_0 = 20°$.

As for C_T, it is possible to see a transition from drag to thrust generation for $\theta_m = 0°$, in the range of $\theta_0 = 0 - 10°$. There also appears to be a peak in thrust generation at $\theta_0 = 10°$. Results for $\theta_m = 10°$ follow a similar distribution, with a plateau at $\theta_0 = 10°$, however the clearly higher lift values seem to be compensated by a loss in thrust production. This can be explained by thinking of adding a mean angle of attack as changing the direction of thrust production: When $\theta_m = 0°$, thrust is aligned with the axial direction, and so it is maximum. When a θ_m is introduced, thrust is now projected in the vertical direction as well. This causes the increase in lift but the reduction of thrust, or increase in drag.

Finally, figure 6.10 represents the same information, but adding the visualization of the standard deviation. For C_L, variation above and below the mean decreases with increased θ_0: as θ_0 increases, $\Delta\alpha_e$ diminishes, so the positive and negative peaks become closer. In C_T there is no clear pattern.

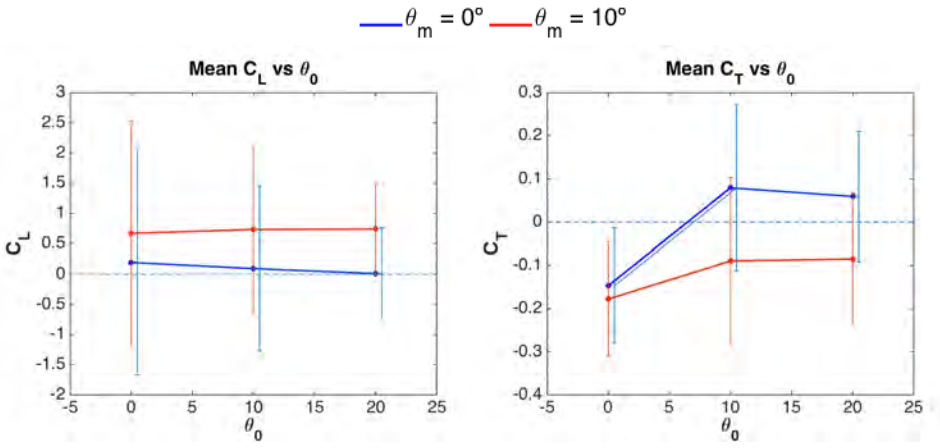

FIGURE 6.10: On the right, $\overline{C_L}$, on the left $\overline{C_D}$ as a function of θ_0 for $\theta_m = 0°$,$\theta_m = 10°$ ($Re = 3600$, $St = 0.2$), with added σ

Note that the σ bars for $\theta_m = 0°$ are slightly shifted so as to not overlap with the $\theta_m = 10°$ bars.

6.4 Lift and Thrust Coefficient Evolution versus Effective Angle of Attack.

The results in this section serve as support for the explanations shown in the previous two. For a better analysis, the results are ordered by θ_m, as the distributions in both C_L and C_T are heavily dependent on this parameter.

Looking at figures 6.11, 6.12 and 6.13, it is easy to see how α_e range is reduced as θ_0 is increased. The table below summarizes the α_e range and the corresponding C_L peaks.

Case	θ_0	α_e *Range*	$C_{L_{max}}$	$C_{L_{min}}$
$C1_{PP,0}$	0°	$-32°$ to 32°	3.0	-2.6
$C3_{MF,0}$	10°	$-22°$ to 22°	2.0	-2.1
$C5_{HF,0}$	20°	$-12°$ to 12°	1.0	-1.2

TABLE 6.4: Peak C_L and α_e range for $\theta_m = 0°$.

Notice how α_e range is symmetric, and thus $C_{L_{max}}$, $C_{L_{min}}$ should be quite close in value in absolute terms.

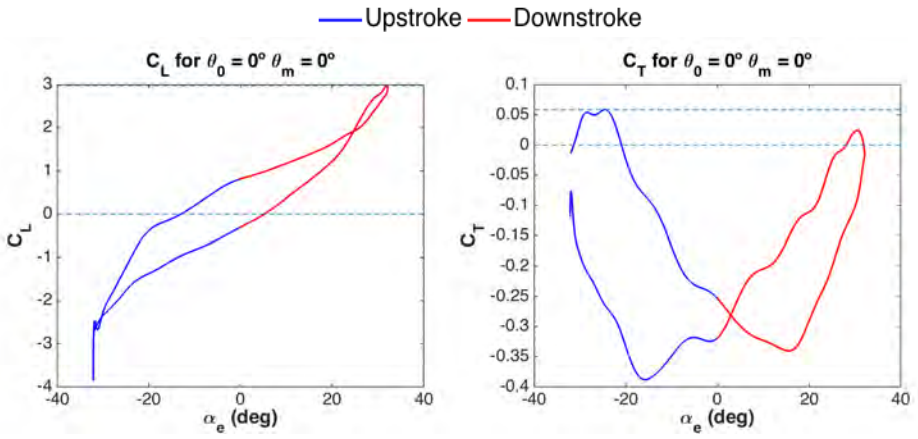

FIGURE 6.11: Evolution of aerodynamic force coefficients over a single cycle for $C1_{PP,0}$ ($Re = 3600$, $St = 0.2$) C_L and C_T as a function of α_e. On the left, C_L, and the right C_T for $\theta_0 = 0°$ and $\theta_m = 0°$

Also interesting is that all three cases seem to show very similar, but opposing distributions in the upstroke and the downstroke. That is, the lobes of the ellipse-like figure are very similar in shape. Of course, this is expected of motions with null mean pitch angle. It supports the idea that indeed upstroke and downstroke are complete mirror images of each other.

In addition, these cases seem to show a wider eccentricity of the ellipse-like plot, when compared to the cases with $\theta_m = 10°$ and equal θ_0. This was seen in the previous section as a wider C_L peak.

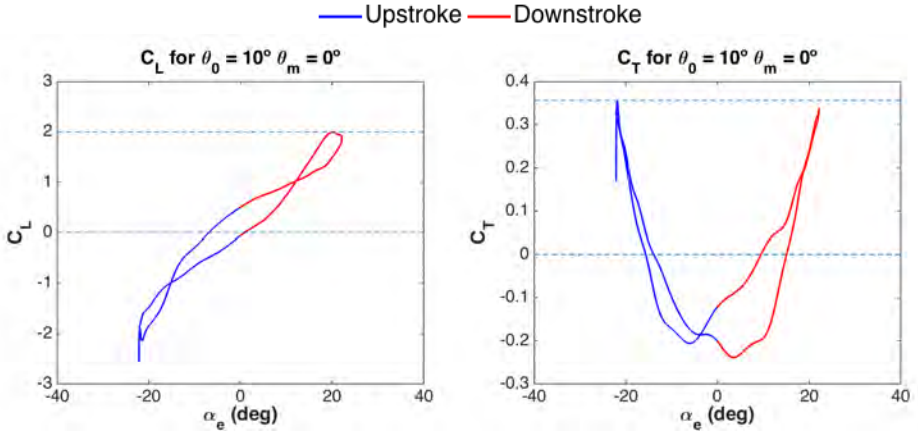

FIGURE 6.12: Evolution of aerodynamic force coefficients over a single cycle for $C3_{MF,0}$ ($Re = 3600$, $St = 0.2$) as a function of α_e. On the left, C_L, and the right C_T for $\theta_0 = 10°$ and $\theta_m = 0°$

In terms of C_T the analysis becomes more difficult, due to the reduced accuracy of the results. However there are some patterns worth mentioning. In cases with $\theta_m = 0°$, there is a clear hint at a symmetry, thrown slightly off likely due to the imprecisions of

the Butterworth filters, due to the delay or lag they present when processing the signal. Also interesting is these are the only cases, save for $\theta_0 = 0°$, pure plunge, which show a thrust producing cycle. They are the only cases showing higher thrust than drag peaks. The thrust peaks are distributed so that they coincide with the highest α_e in terms of absolute value.

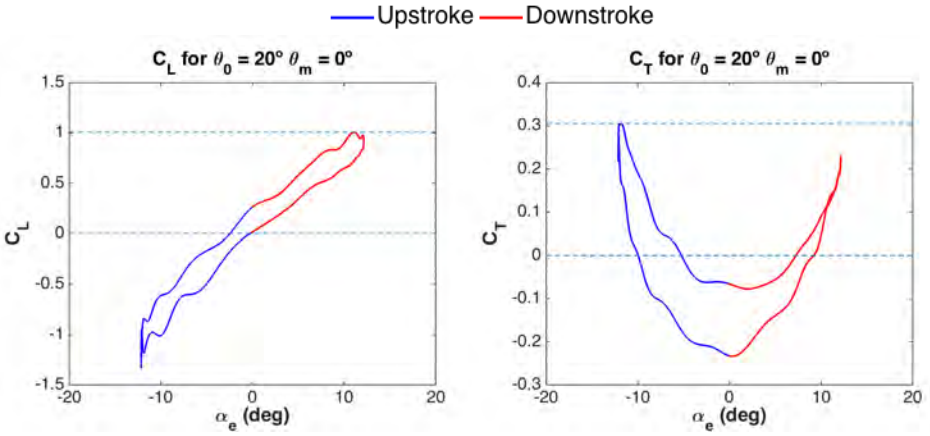

FIGURE 6.13: Evolution of aerodynamic force coefficients over a single cycle for $C5_{HF,0}(Re = 3600,\ St = 0.2)$ as a function of α_e. On the left, C_L, and the right C_T for $\theta_0 = 20°$ and $\theta_m = 0°$

Cases with $\theta_m = 10°$ can be studied in figures 6.14, 6.15 and 6.16. Naturally, the α_e range is equal to that of the previous three cases but shifted up in 10°. The table below summarizes the α_e range and the corresponding C_L peaks.

Case	θ_0	α_e *Range*	$C_{L_{max}}$	$C_{L_{min}}$
$C1_{PP,0}$	0°	−22° to 42°	4.1	-2.8
$C3_{MF,0}$	10°	−12° to 32°	3.1	-0.9
$C5_{HF,0}$	20°	−2° to 22°	2.2	-0.3

TABLE 6.5: Peak C_L and α_e range for $\theta_m = 0°$.

C_L values are proportional to α_e, and so the minimum and maximum values will change accordingly. These cases will therefore display higher $C_{L_{max}}$ and less negative $C_{L_{min}}$ than the previous three.

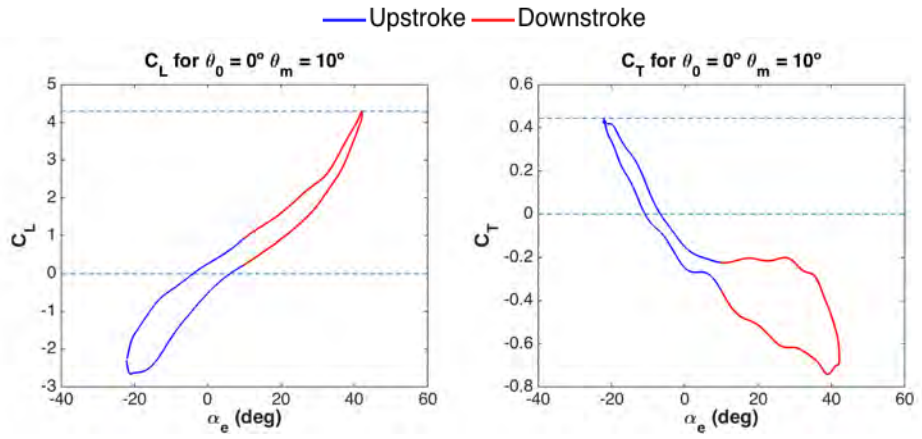

FIGURE 6.14: Evolution of aerodynamic force coefficients over a single cycle for $C2_{PP,10}(Re = 3600,\ St = 0.2)$ as a function of α_e. On the left, C_L, and the right C_T for $\theta_0 = 0$ and $\theta_m = 10$

This asymmetric distribution of lift means the upstroke and downstroke are no longer mirror images of one another. Therefore, it is expected that the lobes of the ellipse are no longer so similar. Instead, the positive lobes are longer than the negative part of the ellipse.

In addition, in the positive lobe, the eccentricity of the ellipse is noticeably more narrow than in $\theta_m = 0°$ cases. This is coherent with the results of section 6.2, where more narrow C_L peaks were observed.

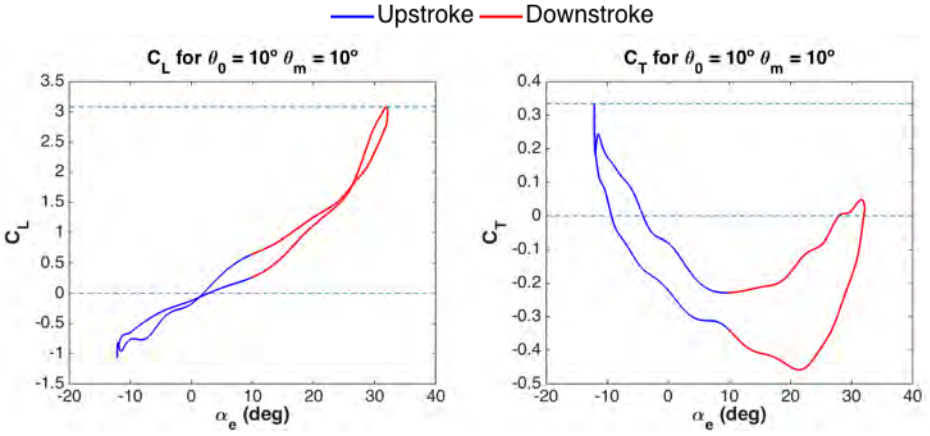

FIGURE 6.15: Evolution of aerodynamic force coefficients over a single cycle for $C4_{MF,10}$ $(Re = 3600,\ St = 0.2)$ as a function of α_e. On the left, C_L, and the right C_T for $\theta_0 = 10°$ and $\theta_m = 10°$

This lack of symmetry is also obvious in C_T plots. Finding a pattern seems complex: in $C2_{PP,10}$ and $C4_{MF,10}$, thrust seems to dominate during the upstroke at the most negative α_e. However in $C6_{HF,10}$ the opposite seems to be true.

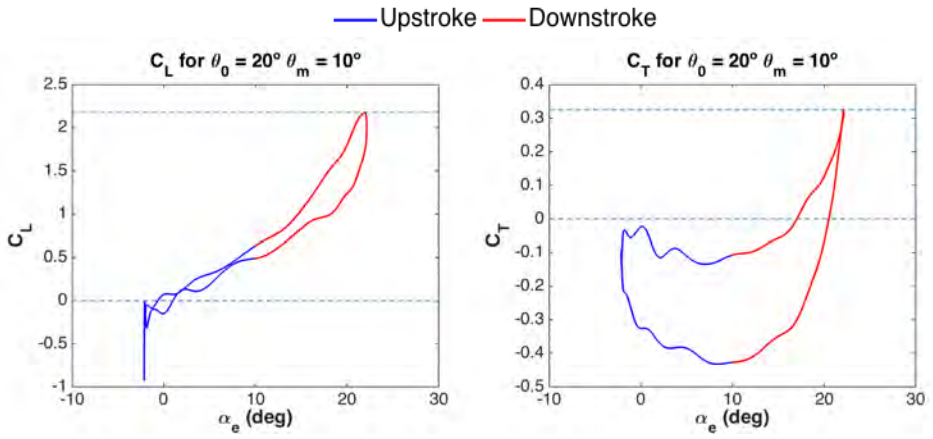

FIGURE 6.16: Evolution of aerodynamic force coefficients over a single cycle for $C6_{HF,10}(Re = 3600,\ St = 0.2)$ as a function of α_e. On the left, C_L, and the right C_T for $\theta_0 = 20°$ and $\theta_m = 10°$

Chapter 7

PIV Experiments: Results

In this chapter, the results of the two PIV experiments will be displayed and analyzed to find accordance with the theory.

The experiments performed correspond with case $C1_{PP,0}$ and $C6_{HF,10}$, whose parameters can be seen in table 6.1. As explained before, the results are heavily dependent on θ_m, so one case with each θ_m was selected.

7.1 Discretization Parameters

In section 5.1, the process of discretizing the cycle was thoroughly explained. The parameters that define this discretization are summarized in the table below:

Oscillation frequency, f:	0.4 Hz
Camera frequency, f_{cam}:	8.1 Hz
Number of velocity fields:	5670

TABLE 7.1: PIV experiment fundamental input data.

These three main parameters render the following discretization values:

Phases per cycle, n_ϕ:	81
Images per phase, snapshots:	70

TABLE 7.2: PIV experiment fundamental dicretization values.

This means each cycle will have 81 data points, or one point per 4.444°, and 70 images per data point to generate an accurate mean phase.

7.2 Symmetric Case

The symmetric case chosen for the first PIV experiment is $C1_{PP,0}$. This case was ran at $Re = 3600$ and $St = 0.2$, with $\theta_0 = 0°$ and $\theta_m = 0°$.

Cases with $\theta_m = 0$ have an especially interesting C_T distribution, so the analysis will be more focused on this parameter.

7.2.1 Case Discretization

The case is carefully discretized to better analyze how the vortical structures affect lift and drag forces.

Figure 7.1 shows this dicretization. The green lines show the t/T values for which there is a rendered vorticity contour. This figure also serves as a reference for C_L and C_T values for each of those t/T.

The displayed t/T snapshots of the flow were chosen to show particularly important or interesting points in the cycle. As such, transition points from upstroke to downstroke and vice versa are represented, with $t/T = 0.25$ and $t/T = 0.75$, respectively. Also important are mid-stroke points, as peak forces are expected at precisely those points. Thus, the mid-point of the downstroke is rendered, with $t/T = 0.5$, as is the mid-point of the upstroke at $t/T = 0 = 1$.

In addition to these important cycle points, two-additional snapshots have been rendered during the lift producing phase, to achieve a more thorough analysis of said phase of the cycle. Thus, $t/T = 0.375$, and $t/T = 0.625$ are also represented. They are the mid-points between transition t/T, and mid-stroke t/T.

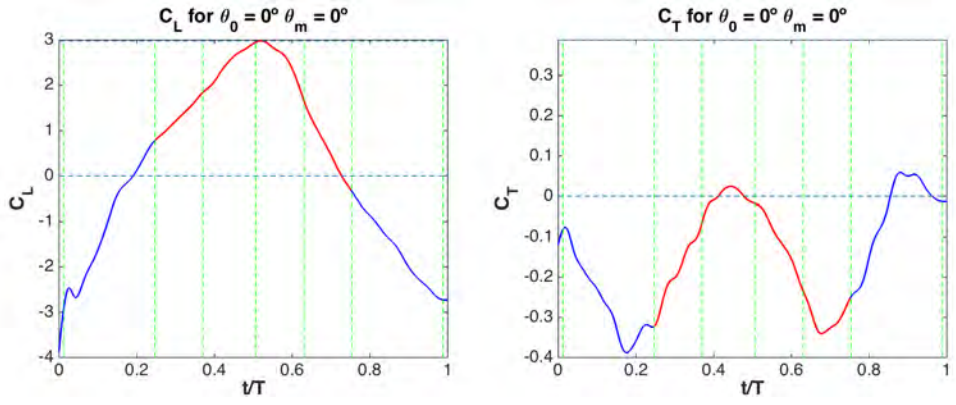

FIGURE 7.1: Discretization of the symmetric case. Green lines show t/T at which a vorticity contour is shown.

Note that the exact values of t/T vary slightly with the ones described. Instead, the closest values acquired in the experiment are displayed.

7.2.2 Results

This case is a pure plunge case, where the geometric angle of attack is kept constant. However, due to the velocity of the plunging wing through the fluid, there is an effective angle of attack, and so aerodynamic forces and vortical structures are expected.

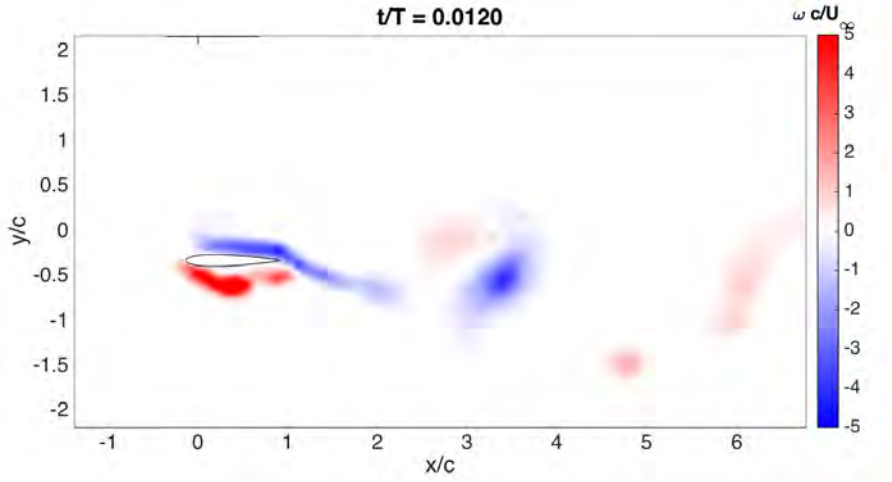

FIGURE 7.2: Vorticity contour for $t/T = 0.0120$, for case $C1_{PP,0}$ ($\theta_0 = 0°$, $\theta_m = 0°$, $Re = 3600$, $St = 0.2$)

In figure 7.2 one can see the initial moments of the cycle, which coincides with the middle of the upstroke. This point displays the most negative effective angle of attack of the motion, and so it also displays the most negative C_L. On the right, it is also possible to see the remnants of one of the von Karman vortices. From the LE of the bottom surface of the wing, emanates a vortex with positive circulation, contributing to this downward, negative lift. From this point forward we should expect an increasing lift, as this bottom surface LEV detaches from the airfoil. As the vortex develops, drag increases.

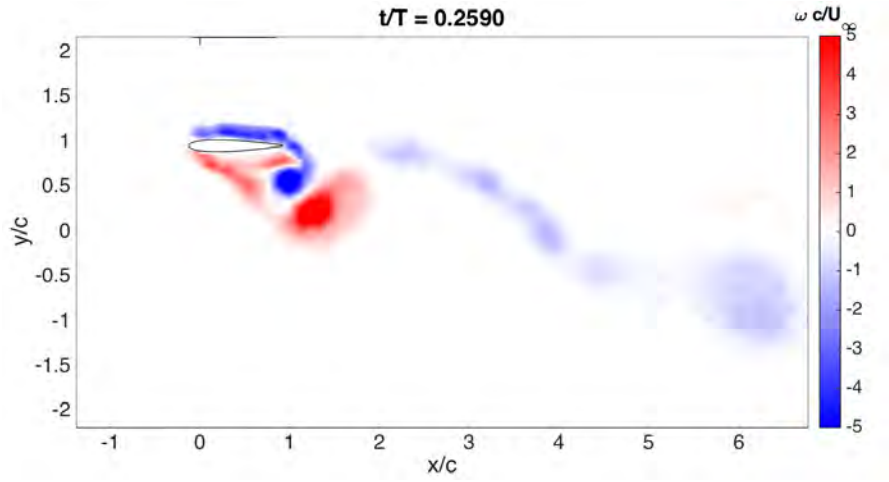

FIGURE 7.3: Vorticity contour for $t/T = 0.2590$, for case $C1_{PP,0}$ ($\theta_0 = 0°$, $\theta_m = 0°$, $Re = 3600$, $St = 0.2$)

As the flow develops, at $t/T = 0.25$ the airfoil reaches the top position. This is the transition from upstroke to downstroke. It is the point with highest drag. At this point, the TEV has developed and pinches off under the LEV, generating the beginning of the von Karman vortex street. As the vortices leave the airfoil, drag decreases. See figure 7.3. The effects of these large vortices may also play a role in the asymmetry of the force distribution mentioned in section 6.2, figure 6.1, where the transition to positive C_L was expected at this upstroke to downstroke transition point, but instead happens earlier. The separation of the bottom LEV increases lift earlier than $t/T = 0.25$.

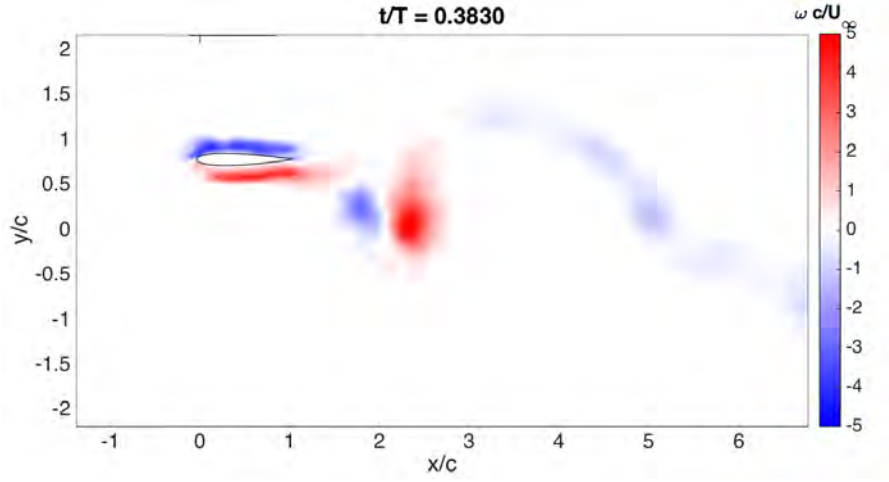

FIGURE 7.4: Vorticity contour for $t/T = 0.3830$, for case $C1_{PP,0}$ ($\theta_0 = 0°$, $\theta_m = 0°$, $Re = 3600$, $St = 0.2$)

Figure 7.4 shows $t/T = 0.3700$, chosen as a midpoint between $t/T = 0.25$ and $t/T = 0.5$, to further study the vortex street. It is possible to see the von Karman vortices are still

strong. This point in time corresponds with the downstroke, so an increase in C_L is justified.

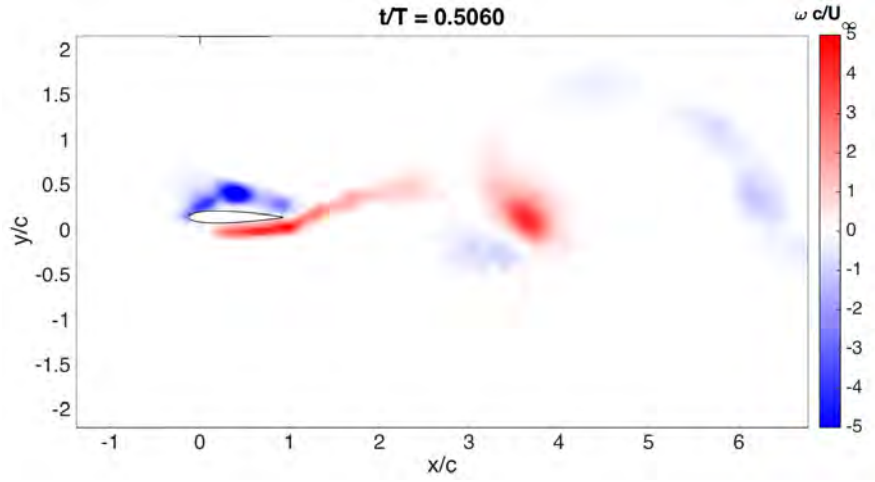

FIGURE 7.5: Vorticity contour for $t/T = 0.5060$, for case $C1_{PP,0}$ ($\theta_0 = 0°$, $\theta_m = 0°$, $Re = 3600$, $St = 0.2$)

At $t/T = 0.5$, shown in figure 7.5, the C_L peak is reached. This is the position with the highest α_e. It is also possible to see the LEV at its maximum circulation over the upper surface of the wing, contributing to this high lift. Moreover, it becomes apparent that indeed this is a perfectly symmetrical case: The flow in this position is identical to figure 7.2 ($t/T = 0$), with the opposing sign in vorticity. This is also the point of peak thrust, but as the LEV further develops and detaches, a decrease is expected.

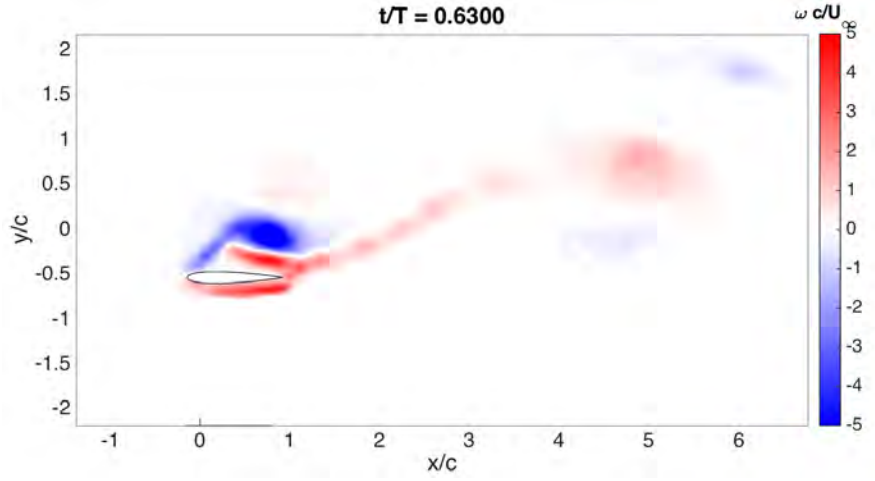

FIGURE 7.6: Vorticity contour for $t/T = 0.6300$, for case $C1_{PP,0}$ ($\theta_0 = 0°$, $\theta_m = 0°$, $Re = 3600$, $St = 0.2$)

At $t/T = 0.6300$, (figure 7.6) it is possible to see precisely this development, and the subsequent increase in drag. During this second phase of the downward stroke, C_L

begins to decrease. It is possible to see how the LEV detaches from the wing, and the first hints at the TEV are visible.

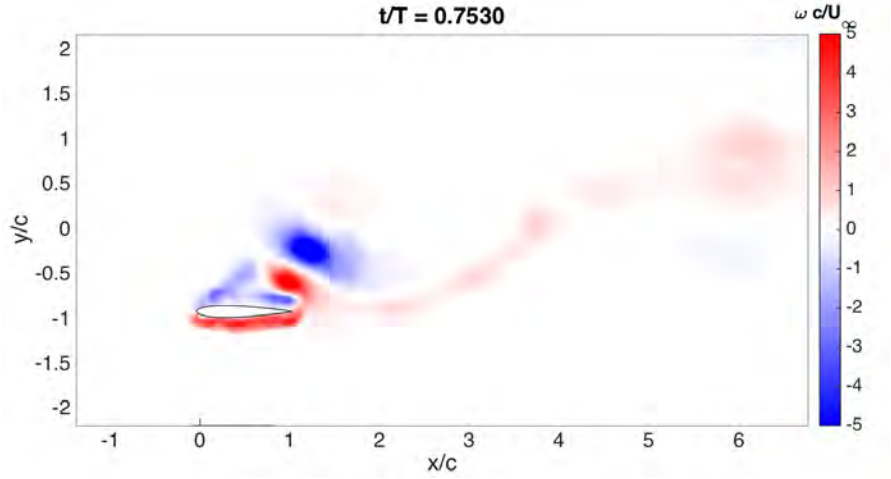

FIGURE 7.7: Vorticity contour for $t/T = 0.7530$, for case $C1_{PP,0}$ ($\theta_0 = 0°$, $\theta_m = 0°$, $Re = 3600$, $St = 0.2$)

As $t/T = 0.7530$, the end of the downstroke is reached, and drag is at its maximum value. Again, but now in a mirror image, the TEV pinches off under the LEV, generating the von Karman street, and beggining the thrust increase phase, which should last until C_T peak at $t/T = 1$.

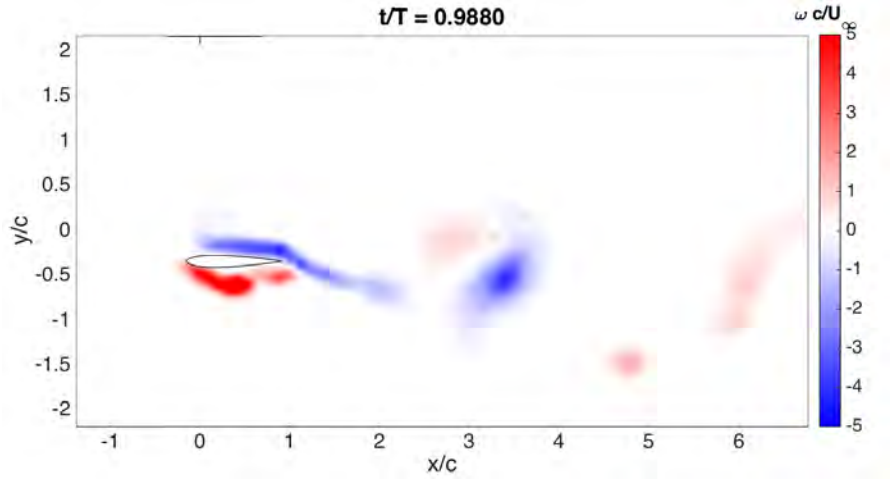

FIGURE 7.8: Vorticity contour for $t/T = 0.9880$, for case $C1_{PP,0}$ ($\theta_0 = 0°$, $\theta_m = 0°$, $Re = 3600$, $St = 0.2$)

Figure 7.8 is nearly identical to $t/T = 0.0012$, as they both mark the beginning and end of the cycle.

7.3 Non-symmetric Case

The non-symmetric case chosen for the second PIV experiment is $C6_{HF,10}$. This case was ran at $Re = 3600$ and $St = 0.2$, with $\theta_0 = 20°$ and $\theta_m = 10°$.

It is interesting as it shows the highest overall $\overline{C_L}$, and the highest $\overline{C_T}$ of the cases with $\theta_m = 10°$.

7.3.1 Case Discretization

The discretization of the case is identical to the previously described instance. A reference point is set at each transition from down/upstroke and vice versa, and in each middle of stroke. Additionally, two more references are set during the downstroke, to have a more detailed look at what occurs during this maximum C_L phase of the cycle.

In summary, references are set at the closest acquired points to $t/T = 0$, 0.25, 0.375, 0.5, 0.625, 0.75, and 1, as shown in figure 7.9.

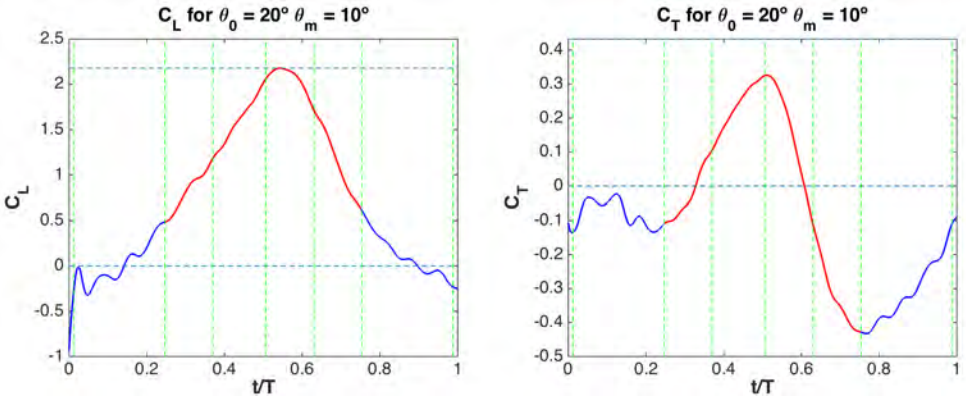

FIGURE 7.9: Discretization of the non-symmetric case. Green lines show t/T at which a vorticity contour is shown.

7.3.2 Results

This second non-symmetric case is interesting because in addition to adding a mean pitch angle, it introduces a pitching amplitude. It should therefore be a more revealing case of flapping wing mechanics.

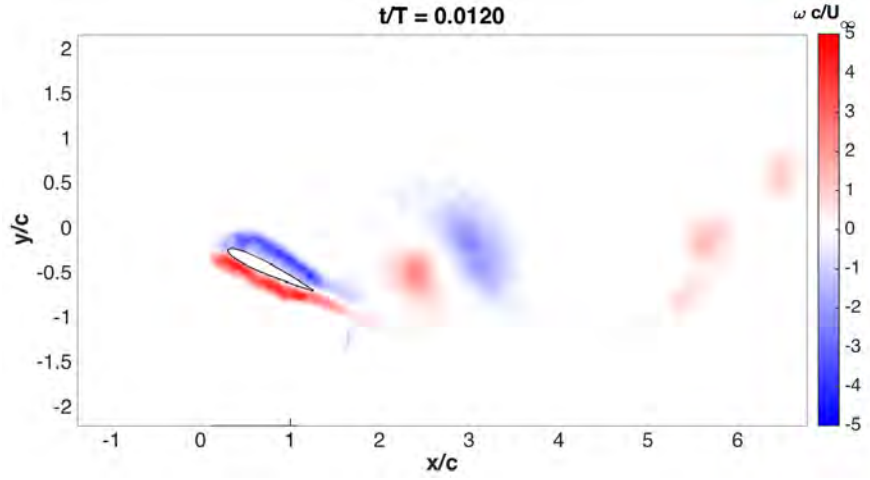

FIGURE 7.10: Vorticity contour for $t/T = 0.0120$, for case $C6_{HF,10}$ ($\theta_0 = 20°$, $\theta_m = 10°$, $Re = 3600$, $St = 0.2$)

The beginning of the cycle corresponds to the middle of the upstroke, and can be seen in figure 7.10. An interesting note from this figure is the clear presence of a von Karman street. During this upstroke, C_L should be low.

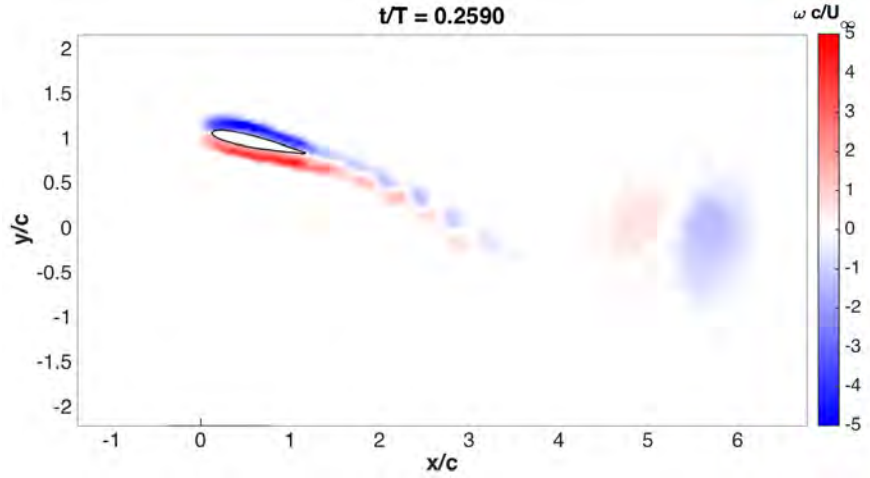

FIGURE 7.11: Vorticity contour for $t/T = 0.2590$, for case $C6_{HF,10}$ ($\theta_0 = 20°$, $\theta_m = 10°$, $Re = 3600$, $St = 0.2$)

Approaching $t/T = 0.25$, transition from upstroke to downstroke, the circulation in the LEV increases, as does C_L. The large von Karman vortices are is still visible, and the airfoil experiences a thrust increase until the middle of the downstroke. A von Karman street made of smaller vortices is also visible piching off the trailing edge of the airfoil.

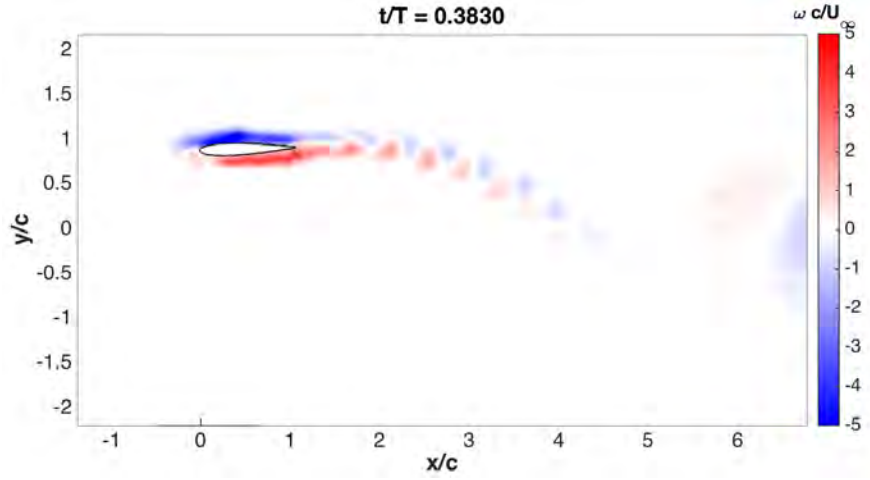

FIGURE 7.12: Vorticity contour for $t/T = 0.3830$, for case $C6_{HF,10}$ ($\theta_0 = 20°$, $\theta_m = 10°$, $Re = 3600$, $St = 0.2$)

In figure 7.12, $t/T = 0.3830$, the circulation continues to increase, and C_L continues to climb. The large von Karman vortices begin to fade, as the flow approaches the dragging phase which will start at the middle of the downstroke.

The middle of the downstroke, seen in figure 7.13, shows the peak C_L, and not coincidentally corresponds to the maximum circulation of the LEV attached to the upper surface of he airfoil. C_T is also at its maximum value, and will begin to decline. The decline in C_L and C_T will correspond with the growth and detachment of the LEV, and the birth of the TEV.

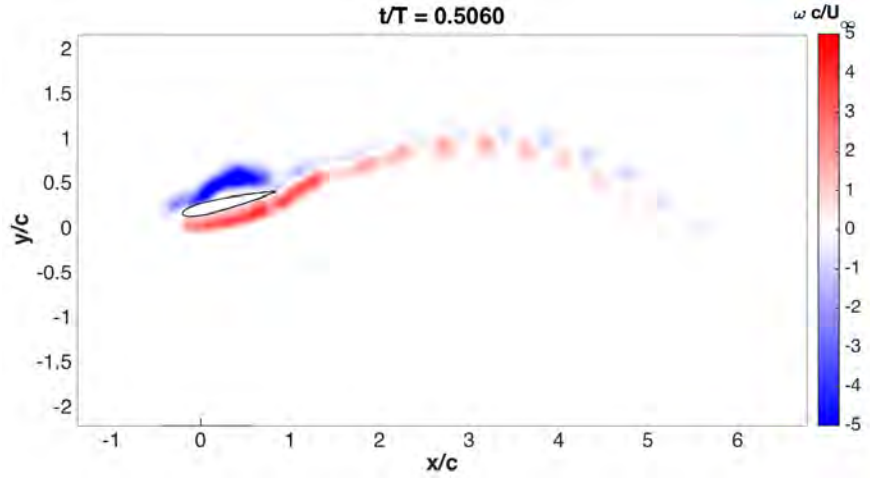

FIGURE 7.13: Vorticity contour for $t/T = 0.5060$, for case $C6_{HF,10}$ ($\theta_0 = 20°$, $\theta_m = 10°$, $Re = 3600$, $St = 0.2$)

Also interesting is through the development of the downstroke until its mid-point, from $t/T = 0.25$ to $t/T = 0.5$ it is possible to see small von Karman vortices in the wake of the airfoil. They are much smaller than the large vortices generated by the shedding of

the LEV and TEV in the transition from upstroke to downstroke. In figure 7.13, the vortex street seems to stop forming.

In the figure below, with $t/T = 0.6300$ the LEV has begun detachment, as the TEV begins its evolution. The small vortex street has indeed stopped forming, as the LEV and TEV grow, increasing drag.

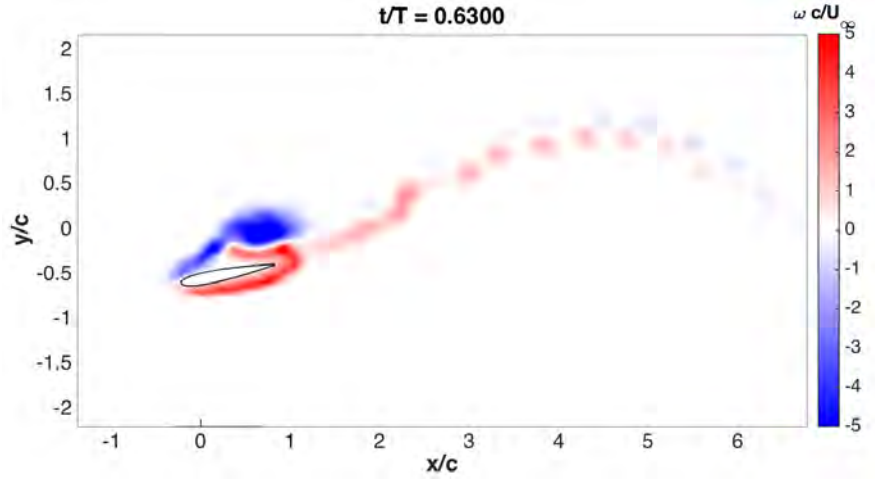

FIGURE 7.14: Vorticity contour for $t/T = 0.6300$, for case $C6_{HF,10}$ ($\theta_0 = 20°$, $\theta_m = 10°$, $Re = 3600$, $St = 0.2$)

When the transition point between downstroke and upstroke begins, at $t/T = 0.75$, the TEV pinching off under the detached LEV is clearly visible. This is the phase of the motion with the highest drag. C_L of course is still diminishing.

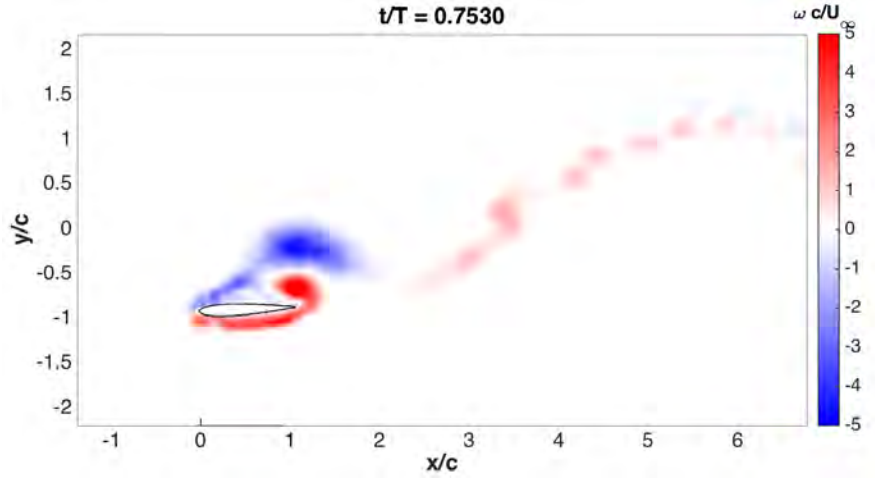

FIGURE 7.15: Vorticity contour for $t/T = 0.7530$, for case $C6_{HF,10}$ ($\theta_0 = 20°$, $\theta_m = 10°$, $Re = 3600$, $St = 0.2$)

As the vortices are shed, C_T increases rapidly once more, marking the end, and beginning of the cycle. Figure 7.16, which represents $t/T = 0.9880$ is therefore almost identical to 7.10, which represents $t/T = 0.0012$.

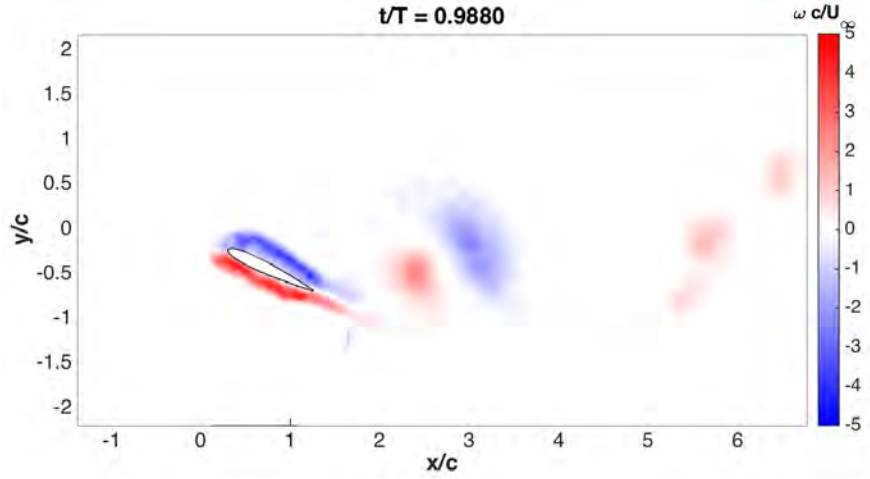

FIGURE 7.16: Vorticity contour for $t/T = 0.9880$, for case $C6_{HF,10}$ ($\theta_0 = 20°$, $\theta_m = 10°$, $Re = 3600$, $St = 0.2$)

None of the cases display an inverse von Karman vortex, as none are thrust producing overall. A PIV study of a thrust producing case may be an interesting option for future analysis.

Chapter 8

Conclusion

With the main objective of the project completed, and once the results have been analyzed, it is time to draw the appropriate conclusions. The experiments were ran with a fixed phase lag, ϕ of 90°, $Re = 3600$, $St = 0.2$, $k = 0.1\pi$ and $h_0/c = 1$, so the parametric study is based on the remaining free parameters, namely θ_0 and θ_m.

The analysis of force coefficients over the time evolution of the cycle rendered interesting observations in the effect of the free parameters on lift and thrust production. In the case of C_L, several observations were noted: As a general rule, and in accordance with the theory, cycles with null mean pitch angle should not produce lift overall. The symmetry of the motion means the flow in one surface of the wing has an analogous flow in the opposing surface with opposing vorticity at some point in the cycle, leading to $\overline{C_L} = 0$. That is, points of the cycle with a phase shift of $t/T = 0.5$, have approximately equal values of C_L, but opposing sign. These results did present some errors, but the relationship of the errors with the standard deviation of C_L suggests it is a systematic error within the expected range. Cases with $\theta_m = 10°$ did produce lift, and lift production varied with pitching amplitude θ_0. While increasing θ_0 reduces the value of the peaks, it does not necessarily decrease $\overline{C_L}$. In fact, in the transition from $\theta_0 = 0°$ to $\theta_0 = 10°$, a notable increase is noted. The transition from $\theta_0 = 10°$ to $\theta_0 = 20°$ shows just a slight rise.

These results are further backed by the analysis of the forces as a function of effective angle of attack, α_e. Looking at the α_e histories for each cycle, a clear correlation is noted. Cases with $\theta_m = 0°$ show anti-symmetric angle of attack, meaning each point in the cycle has an equal angle of attack with opposing sign at +0.5 phase. Cases with $\theta_m = 10°$, which is essentially shifting positively the curve by 10° do not display this property and thus produce lift.

In terms of C_T, the importance of θ_m is evident. Only cases with $\theta_m = 0°$ are capable of thrust production, meaning there is a clear trade-off between lift and thrust production. Theoretically this makes sense, as adding a mean angle of attack means projecting the thrust not just horizontally, but also vertically, increasing lift but reducing the horizontal thrust component. Nonetheless, θ_0 also has effects on thrust production. For both $\theta_m = 0°$ and $\theta_m = 10°$, there is a notable decrease in drag the higher the θ_0, with a particularly high jump in the transition from $\theta_0 = 0°$ to $\theta_0 = 10°$, much like with C_L.

From these conclusions, it appears that case $C6_{HF,10}$ is the better balance between lift and drag, although just slightly better than $C4_{MF,10}$. This means that if θ_0 is a design limit, $C4_{MF,10}$ might be a good option.

The study of the flow structure also renders notable observations. As backed by a number of previous investigations described in the literature review, LEV seems to play a major role in lift enhancement during the downstroke motion of the wing. The development of the LEV as well as the TEV, and the shedding of these vortivces appears to also play a role in drag evolution. During the growing phase of the LEV, an increase in lift is displayed. But, past the mid-point of the downstroke, the growing and detaching LEV, coupled with the birth of the TEV seem to drastically increase drag, which decreases again as the vortices are shed from the airfoil.

As a suggestion for future related projects, it would be advised to perform a PIV analysis of a thrust producing case, such as case $C3_{MF,0}$, with $\theta_0 = 10°$ and $\theta_m = 0°$, in order to be able to observe and study the reverse von Karman street. In addition, performing the same PIV experiments as force coefficient experiments may shed some light on the less intuitive results, for example $C4_{MF,10}$ and $C6_{HF,10}$ having essentially equal $\overline{C_L}$, or cases $C4_{MF,10}$ and $C6_{HF,10}$, and $C3_{MF,0}$ and $C5_{HF,0}$ having very similar $\overline{C_T}$.

Chapter 9

Project Planning and Budget

This chapter covers the project management aspect of the development of the thesis. As such, it describes the time evolution of the project, as well as an estimate of the total cost, in an effort to serve as a baseline for future similar projects to improve upon.

9.1 Project Planning

The planning of the project could be separated in 7 different phases, spanning over the course of 7 months. Being an experimental project, the variability of the projected time and the actual time is quite high, as unexpected issues are common.

- **Research and Documentation:** This first step of the project involved getting familiar with the project at hand. The result of this documentation phase of the project is the literature review. Although the bulk of the documentation was performed during the first days since assignment, research was continuously performed throughout the project.
- **First experimental activities:** The motion system was set up at the Fluid Mechanics laboratory at Universidad Carlos III de Madrid. The first data sets were acquired. The purpose of these experiments were two: Familiarizing with the control of the motion system and data capture process, and identifying - and fixing - noise errors.
- **Force processing code development:** Developing the scripts to filter noise, and manage the data sets to obtain aerodynamic force coefficients, and display the results appropriately.

- **Experimental setup in new water tunnel:** The motion system was disassembled, transported and installed in the new, larger water tunnel of the Aerospace Engineering Group. The lid was modified and tested to withstand necessary pressurization. PIV was setup on the newly built structure, and tunnel was calibrated.
- **Definitive experimental activity:** The definitive cases were defined and carried out. Several iterations were necessary due to sensor saturation issues, noise, trigger failures, and pressure failure.
- **PIV processing code development:** The scripts to manage and process PIV data was written, to adequately display the results of the PIV experiments.
- **Report writing:** The final report with the results of the experiments was written.

The total time expenditure of each phase and the total project time is summarized in table 9.1

Activity	**Time [h]**
Research and documentation	20
First experimental activity	25
Force processing code development	35
New water channel setup	40
Definitive experimental activity	100
PIV post-processing code development	30
Report writing	110
Total:	**360**

TABLE 9.1: Total time expenditure of the thesis development.

9.2 Budget

The budget for the project summarizes the estimated costs of running the experiments and completing the analysis. This includes the cost of any materials, existing or acquired, software licenses, computing time, and personnel costs. Total costs are rounded to the nearest ten.

9.2.1 Equipment

These accrue the cost of acquired materials, as well as the depreciation value of existing equipment, assuming a linear depreciation with the lifetime of the equipment.

Equipment	Cost	Amortization [y.]	Cost [€]/year	Use	Total Cost [€]
Personal Laptop	1200	5	240	220 h	20
Water Channel	180000	5	36000	1 month	3000
PIV System	15000	5	3000	2 weeks	115
Motion System	10000	5	2040	1 month	170
Force Measuring	11900	5	2380	1 month	200
Total:					3510*

TABLE 9.2: Depreciation Equipment Costs.*Total rounded to nearest 10.

Material	Cost/Unit	Quantity [Units]	Total Cost [€]
Plexiglas lid	250	1	250
Expendables	-	-	500
Total:			750

TABLE 9.3: Acquired materials cost.

9.2.2 Utilities

This is an estimation of the overhead utilities cost associated with running the water tunnel and devices.

Utility	Cost/Unit	Quantity [Units]	Total Cost [€]
Water	1.6 €/m^3	70m^3	112
Electricity	0.18 €/kWh	1650kWh	297
Total:			410*

TABLE 9.4: Utilities cost. *Total rounded to the nearest 10.

9.2.3 Personnel

The costs associated with the time of the Bachelor's Degree student involved in the experiment.

Personnel	Cost [€]/h	Hours [Units]	Total Cost [€]
BSc. Student	20	360	7200
Total:			7200

TABLE 9.5: Personnel cost.

9.2.4 Software

Software costs include the costs of student licenses for software utilized for the development of the thesis, for both data acquisition and post processing.

Software	Total Cost [€]
Matlab	500
LabView	80
Total:	580

TABLE 9.6: Software cost.

9.2.5 Total Costs

The summation of the total cost of tables 9.2 through 9.7 is displayed below. This is a summary of the total cost of the project.

Category	Total Cost [€]
Equipment	4260
Utilities	410
Personnel	7200
Software	580
Total:	12450

TABLE 9.7: Total cost.

Appendix A

An Appendix

This appendix includes plots and figures whose analysis do not necessarily add value to the study, but that may be of interest to the reader.

A.1 Lift Coefficient versus Drag Coefficient

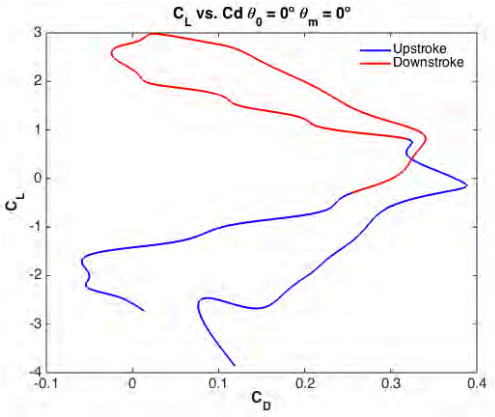

FIGURE A.1: C_L versus C_D ($Re = 3600$, $St = 0.2$) for $\theta_0 = 0$ and $\theta_m = 0$

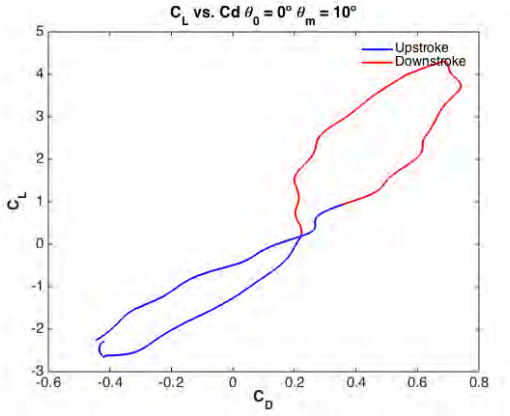

FIGURE A.2: C_L versus C_D ($Re = 3600$, $St = 0.2$) $\theta_0 = 0$ and $\theta_m = 10$

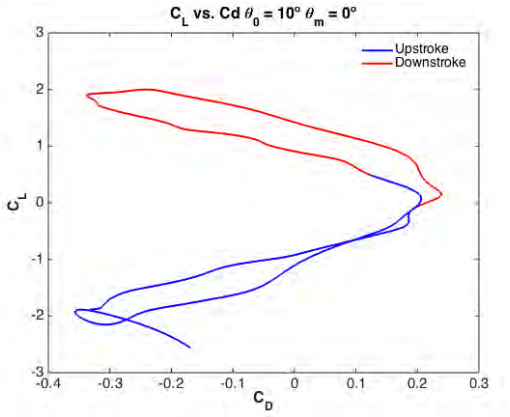

FIGURE A.3: C_L versus C_D ($Re = 3600$, $St = 0.2$) for $\theta_0 = 10$ and $\theta_m = 0$

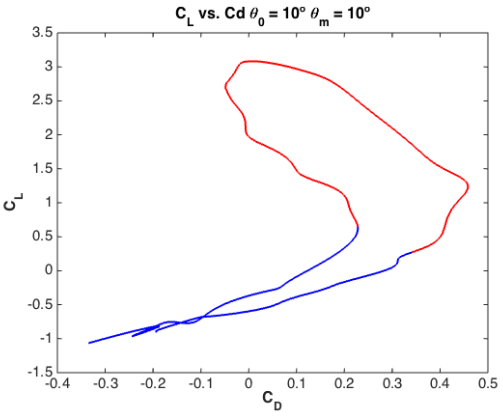

FIGURE A.4: C_L versus C_D ($Re = 3600$, $St = 0.2$) for $\theta_0 = 10$ and $\theta_m = 10$

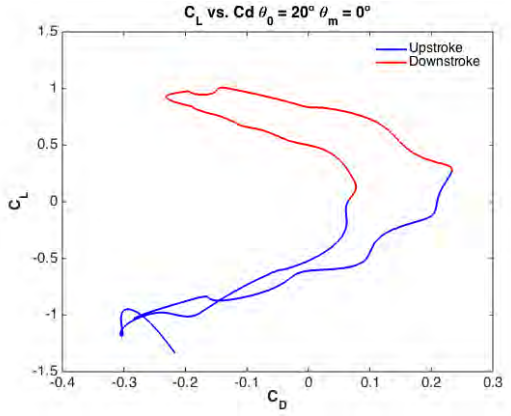

FIGURE A.5: C_L versus C_D ($Re = 3600$, $St = 0.2$) for $\theta_0 = 20$ and $\theta_m = 0$

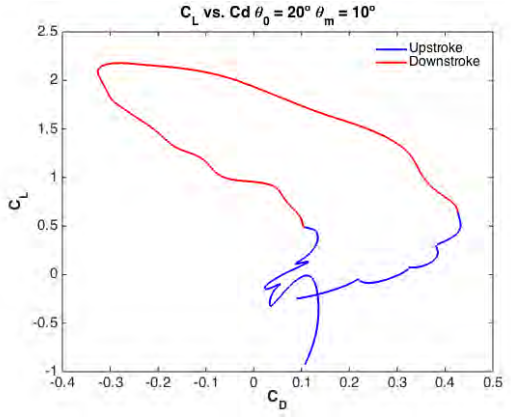

FIGURE A.6: C_L versus C_D ($Re = 3600$, $St = 0.2$) for $\theta_0 = 20$ and $\theta_m = 10$

Bibliography

[1] Michael H Dickinson and Karl G Gotz. Unsteady aerodynamic performance of model wings at low reynolds numbers. *Journal of Experimental Biology*, 174(1): 45–64, 1993.

[2] Rafal Żbikowski. On aerodynamic modelling of an insect–like flapping wing in hover for micro air vehicles. *Philosophical Transactions of the Royal Society of London A: Mathematical, Physical and Engineering Sciences*, 360(1791):273–290, 2002.

[3] SA Ansari, R Żbikowski, and K Knowles. Non-linear unsteady aerodynamic model for insect-like flapping wings in the hover. part 1: methodology and analysis. *Proceedings of the Institution of Mechanical Engineers, Part G: Journal of Aerospace Engineering*, 220(2):61–83, 2006.

[4] Yeon Sik Baik, Luis P Bernal, Kenneth Granlund, and Michael V Ol. Unsteady force generation and vortex dynamics of pitching and plunging aerofoils. *Journal of Fluid Mechanics*, 709:37–68, 2012.

[5] JC S. Lai and MF Platzer. Jet characteristics of a plunging airfoil. *AIAA journal*, 37(12):1529–1537, 1999.

[6] Steve Connor. How a hummingbird in love can move faster than a fighter jet. June 2009. URL http://www.independent.co.uk/news/science/how-a-hummingbird-in-love-can-move-faster-than-a-fighter-jet-1701103.html.

[7] Alexander P Willmott and Charles P Ellington. The mechanics of flight in the hawkmoth manduca sexta. i. kinematics of hovering and forward flight. *Journal of Experimental Biology*, 200(21):2705–2722, 1997.

[8] Pablo Moral Maroto. Design and water tunnel testing of a flapping wing. 2015.

[9] Richard Knoller. *Die gesetze des luftwiderstandes*. Verlag des Österreichischer Flugtechnischen Vereines, 1909.

[10] A. Betz. Ein beitrag zur erklaerung des segelfluges. 1912.

[11] R. Katzmayr. Effect of periodic changes of angle of attack on behavior of airfoils. *NACA TM 147*, 1922.

[12] W. Birnbaum. Das ebene problem des schlagenden fluegels, zeitschrift fuer angewandte mathematik und mechanik. 1924.

[13] T von Karman and JM von Burgers. General aerodynamic theory, perfect fluids. aerodynamic theory. durand ed. vol. ii, 1934.

[14] T Theodorsen. General theory of aerodynamic instability and the mechanism of flutter, naca report 496, us nat. *Advisory Committee for Aeronautics, Langley, VA*, 13, 1935.

[15] I. E. Garrick. Propulsion of a flapping and oscillating airfoil. *NACA, Rept. 567*, 1936.

[16] E. C. Polhamus. A concept of the vortex lift of sharp-edge delta wings based on a leading-edge-suction analogy. 1966.

[17] JM Anderson, K Streitlien, DS Barrett, and MS Triantafyllou. Oscillating foils of high propulsive efficiency. *Journal of Fluid Mechanics*, 360:41–72, 1998.

[18] Charles P Ellington. The novel aerodynamics of insect flight: applications to micro-air vehicles. *Journal of Experimental Biology*, 202(23):3439–3448, 1999.

[19] Charles P Ellington, Coen Van Den Berg, Alexander P Willmott, and Adrian LR Thomas. Leading-edge vortices in insect flight. 1996.

[20] Sanjay P Sane and Michael H Dickinson. The control of flight force by a flapping wing: lift and drag production. *Journal of experimental biology*, 204(15):2607–2626, 2001.

[21] Wei Shyy, Hikaru Aono, Satish Kumar Chimakurthi, P Trizila, C-K Kang, Carlos ES Cesnik, and Hao Liu. Recent progress in flapping wing aerodynamics and aeroelasticity. *Progress in Aerospace Sciences*, 46(7):284–327, 2010.

[22] Wei Shyy, Hikaru Aono, Chang-kwon Kang, and Hao Liu. *An introduction to flapping wing aerodynamics*, volume 37. Cambridge University Press, 2013.

[23] Yeon Sik Baik, Jonathan M Rausch, Luis P Bernal, Wei Shyy, and Michael Ol. Experimental study of governing parameters in pitching and plunging airfoil at low reynolds number. In *48th AIAA aerospace sciences meeting including the new horizons forum and aerospace exposition*, pages 2010–388, 2010.

[24] CW Pitt Ford and Holger Babinsky. Lift and the leading-edge vortex. *Journal of fluid mechanics*, 720:280–313, 2013.

[25] Grand View Research. Commercial drone market analysis by product, by application and segment forecasts to 2022. January 2016. URL http://www.grandviewresearch.com/industry-analysis/global-commercial-drones-market.

[26] Amazon prime air homepage. URL https://www.amazon.com/b?node=8037720011.

[27] ATI Industrial Automation. Force/torque sensor: Nano17 manual. URL http://www.ati-ia.com/company/NewsArticle.aspx?id=310182740.